IOP Publishing and International Atomic Energy Agency Nuclear Fusion
Nucl. Fusion **53** (2013) 104001 (18pp) doi:10.1088/0029-5515/53/10/104001

DIII-D research towards resolving key issues for ITER and steady-state tokamaks

D.N. Hill[1] **and the DIII-D Team**[2]

[1] Lawrence Livermore National Laboratory, Livermore, CA 94551, USA
[2] General Atomics, PO Box 85608, San Diego, CA 92186-5608, USA

E-mail: hilldn@fusion.gat.com

Received 7 November 2012, accepted for publication 21 March 2013
Published 26 September 2013
Online at stacks.iop.org/NF/53/104001

Abstract
The DIII-D research program is addressing key ITER research needs and developing the physics basis for future steady-state tokamaks. Pellet pacing edge-localized mode (ELM) control in the ITER configuration reduces ELM energy loss in proportion to $1/f_{\mathrm{pellet}}$ by inducing ELMs at up to 12× the natural ELM rate. Complete suppression of ELMs with resonant magnetic perturbations has been extended to the q_{95} expected for ITER baseline scenario discharges, and long-duration ELM-free QH-mode discharges have been produced with ITER-relevant co-current neutral-beam injection (NBI) using external $n = 3$ coils to generate sufficient counter-I_{p} torque. ITER baseline discharges at $\beta_{\mathrm{N}} \sim 2$ and scaled NBI torque have been maintained in stationary conditions for more than four resistive times using electron cyclotron current drive (ECCD) for tearing mode suppression and disruption avoidance; active tracking with steerable launchers and feedback control catch these modes at small amplitude, reducing the ECCD power required to suppress them. Massive high-Z gas injection into disruption-induced 300–600 kA 20 MeV runaway electron (RE) beams yield dissipation rates ∼10× faster than expected from e–e collisions and demonstrate the possibility of benign dissipation of such REs should they occur in ITER. Other ITER-related experiments show measured intrinsic plasma torque in good agreement with a physics-based model over a wide range of conditions, while first-time main-ion rotation measurements show it to be lower than expected from neoclassical theory. Core turbulence measurements show increased temperature fluctuations correlated with sharply enhanced electron transport when $\nabla T_{\mathrm{e}}/T_{\mathrm{e}}^{-1}$ exceeds a critical-gradient scale length. In H-mode, data show the pedestal height and width growing between ELMs with ∇P at the computed kinetic-ballooning limit, in agreement with the EPED model. Successful modification of a neutral-beam line to provide 5 MW of adjustable off-axis injection has enabled sustained operation at $\beta_{\mathrm{N}} \sim 3$ with broader current and pressure profiles at higher q_{min} than previously possible, though energy confinement is lower than expected. Initial experiments aimed at developing integrated core and boundary solutions demonstrated heat flux reduction using enhanced edge radiation from neon injection and innovative divertor geometries (e.g. snowflake configuration).

1. Introduction

The DIII-D Research Program has made significant advances in developing the physics understanding and operational experience needed to ensure the success of ITER. By simulating candidate-operating scenarios in both experiments and modelling with increasing fidelity, this research addresses many of the research needs identified by ITER [1]. Targeted research aims to demonstrate relevant solutions and the scientific basis for avoiding and controlling transient events such as edge-localized modes (ELMs) and disruptions which can limit ITER's reliability.

Many of the results reported here capitalize on several new DIII-D capabilities brought into operation over the past two years. These include 5 MW of variable ($0 \leqslant \rho \leqslant 0.5$) co-current off-axis neutral-beam injection (NBI) (out of 15 MW co-I_{p} and 5 MW counter-I_{p} total beam injection power) for improved current and pressure profile control, 3.4 MW electron cyclotron current drive (ECCD) power with feedback-controlled real-time steering for tearing mode control, high rep-rate (up to 60 Hz) pellet injectors for ELM-control experiments, and boron-filled shell pellets for disruption mitigation. New or significantly improved diagnostics such as microwave Doppler backscattering (DBS) for core turbulence measurements, main-ion rotation measurements, and high-rep-rate high-resolution edge Thomson scattering to observe the evolution of the H-mode pedestal provide enhanced capability for validating simulation codes which are expected to predict

ITER performance and guide scenario development. In aggregate, these capabilities enable DIII-D to serve as a research platform to qualify advanced operating modes for new superconducting long-pulse tokamaks and for ITER's steady-state mission.

The organization of this paper is as follows. Section 2 summarizes progress on developing ELM control for ITER and how improved understanding of the H-mode pedestal informs the research. In section 3 we discuss progress on disruption mitigation and section 4 covers research in support of the $Q = 10$ ITER mission, including tearing mode control, QH-mode developments, and error field correction (EFC). Section 6 covers research directed towards developing predictive capability for burning plasma experiments (pedestal scaling, core transport including intrinsic rotation, the H-mode transition, and fast ions). Then in section 7 we discuss results on advanced tokamak (AT) development using OANBI, with section 8 providing a description of work producing integrated core-boundary solutions. Future research plans for DIII-D are briefly discussed in the concluding section.

2. ELM control and the physics of the pedestal

ELM control is needed for ITER to achieve its fusion goals without frequent replacement of its divertor components. DIII-D is developing both approaches to ELM control planned for ITER: ELM suppression by application of edge-resonant magnetic perturbations (RMPs) [2, 3], and pellet pacing [4] to reduce transient heat loads by increasing ELM frequency. In addition, the DIII-D program continues working to develop the physics basis for naturally ELM-free QH-mode [5], which may be an attractive operating mode for ITER. QH-mode will be discussed in section 4.

In our most recent experiments, the range in edge safety factor (q_{95}) for RMP ELM suppression was extended down from $q_{95} \sim 3.7$ to that expected for ITER baseline discharges operating at $I/aB = 1.4$, or $q_{95} \sim 3.4$. Complete ELM suppression was maintained for 3.5 s ($\sim 45\tau_E$) at ITER relevant pedestal collisionality ($\nu* \leqslant 0.1$) with feedback control of the neutral-beam heating power keeping $\beta_N > 1.8$ as shown in figure 1 [6]. These experiments used an ITER-similar lower-single null shape with $\kappa = 1.8$, $\delta_{up} = 0.4$, $\delta_x = 0.79$ that has the outer divertor strike point positioned to provide particle exhaust with the divertor cryopump (figure 2). Key to extending ELM suppression to lower safety factor appears to be use of only a single row of internal coils (I-coils) above the plasma midplane to produce $n = 3$ perturbations, unlike earlier experiments which used two toroidal rows of I-coils (one above and one below the midplane) to produce the $n = 3$ perturbations. Use of a single toroidal row of coils yields $n = 3$ vacuum-field perturbations with a broader range of poloidal mode numbers (m) than does a single row. However, why this change in spectrum yields ELM suppression at lower q_{95} is not well understood, as vacuum calculations with the SURFMN code [7] (which decomposes the 3D perturbations into Fourier components on flux surfaces) show only modest changes to the flux-surface-average resonant components of the applied field going from double rows to a single row of coils. Analysis of the differences when including the full plasma response in the calculations is in progress.

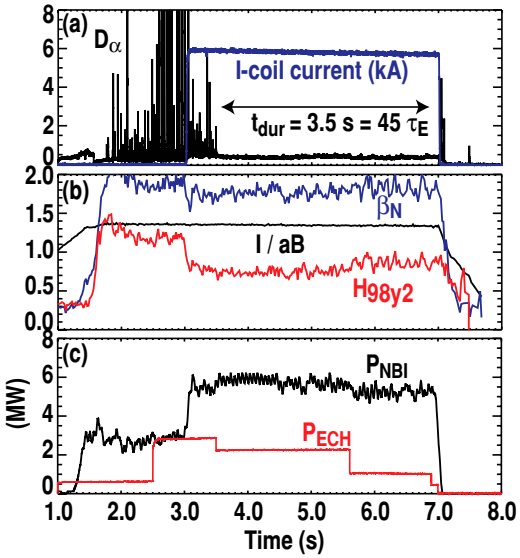

Figure 1. Example discharge showing $n = 3$ RMP ELM suppression in DIII-D at ITER I/aB and low ν^* with ITER-like shape (#150458). (a) Divertor H_α and RMP coil current showing complete suppression after 3.5 s. (b) Similarity to key discharge parameters in ITER. (c) Neutral beam and EC heating power.

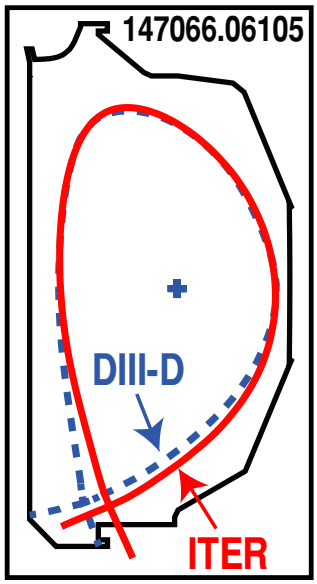

Figure 2. DIII-D plasma shape for RMP ELM suppression experiments (dashed), compared to scaled ITER scenario 1 shape. Outer divertor strike point positioned to provide density control by divertor pumping.

To maintain complete ELM suppression for the duration of the discharge, it was important to avoid growth of tearing modes and other internal MHD activity (e.g. fishbones and large sawteeth) which are often observed when simulating ITER Scenario 2 discharge (e.g. when matching ITER's β_N, q_{95} and shape), independent of the application of the RMP. This was accomplished using ECCD broadly deposited around the $q = 3/2$ surface (figure 1(c)), though the combined application of the ECCD and RMP caused a significant drop in confinement from $H_{98y2} \sim 1.1$–0.75 in the early H-mode phase of this discharge (figure 1(b)). In related experiments, ELM suppression with $n = 2$ RMPs at low ITER-like

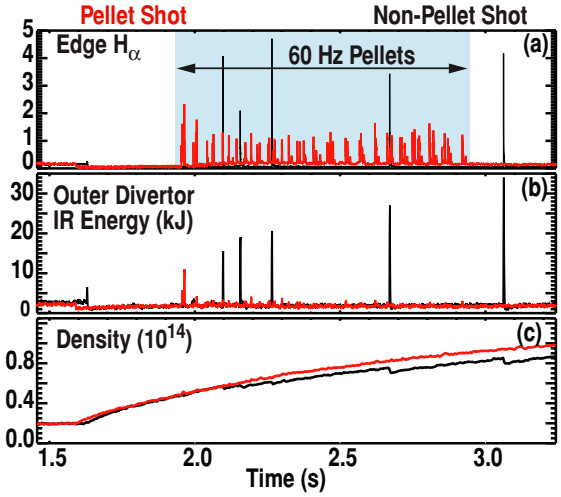

Figure 3. ELM pacing with 1.3 mm deuterium pellets; no pellets (black) versus 60 Hz pellets (red). (*a*) Outer SOL H_α brightness shows variation in pellet timing due to variations in guide tube transit time. (*b*) Integrated outer divertor ELM energy pulse ($\iint 2\pi Rq(R)\mathrm{d}R\mathrm{d}t$). (*c*) Line-average density.

collisionality has also been demonstrated, extending previous results from ASDEX-U showing suppression using $n = 2$ at high collisionality [8].

During initial physics operation and commissioning of control systems, ITER will use only hydrogen or helium and it will be important for ITER to demonstrate successful ELM control during this initial non-nuclear operating phase. RMP ELM suppression experiments with high fractions of helium (10–35%) were carried out using $n = 3$ perturbations in discharges with $q_{95} = 3.4$ and having an ITER similar shape. Complete ELM suppression was only obtained when the core-average helium fraction was less than 25%, possibly due to high collisionality from a lack of density control resulting from the inability of the divertor cryopump to pump helium. We expect that future experiments using argon-frosting on the divertor cryopump will provide adequate density control with much higher fractions of helium to resolve this issue.

ELM pellet pacing experiments using small (0.9–1.3 mm) deuterium pellets show that the ELM frequency can be increased significantly, producing a corresponding decrease in the divertor energy pulse, computed from a running 2 ms time integral of the total divertor heat flux at the outer divertor strike point, $\iint 2\pi Rq(R)\,\mathrm{d}R\,\mathrm{d}t$, as shown in figure 3(*b*). The pellets were injected at a rate of up to 60 pellets s^{-1} into an ITER-shaped plasma with $\beta_N = 1.8$ at $q_{95} = 3.5$, achieving up to 12× higher ELM frequency and a strong reduction in impurity content with little impact on core fueling and energy confinement ($H_{98y2} \sim 0.9$–1.0). The plasmas were operated near the H-mode power threshold to keep the natural ELM rate (~5 Hz) well below the maximum possible pellet injection rate. In these experiments, three 20 Hz pellet injectors were used together to inject 20 pellets s^{-1} at ~150 m s^{-1} on the low-field side midplane and 20 + 20 = 40 pellets s^{-1} through the outer scrape-off layer (SOL) just above the X-point (similar to the planned ITER geometry). Significantly, both the peak divertor heat flux measured by IR thermography and total divertor energy pulse (assuming toroidal symmetry) decreases at least as fast as $1/f_{\mathrm{pellet}}$ [4], as shown in figure 4, similar to

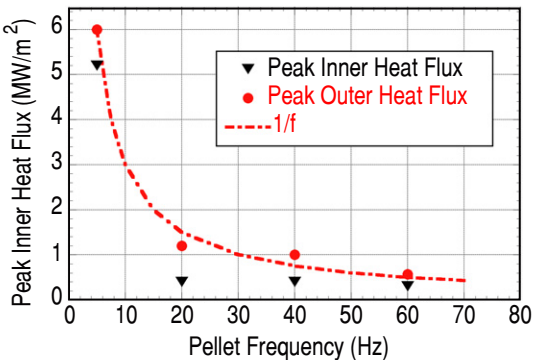

Figure 4. Peak divertor heat flux versus deuterium pellet rate, showing $1/f$ dependence. Without 1.3 mm deuterium pellets, ELMs naturally occur at 5 Hz rate.

the usual relation between naturally occurring ELM size and frequency.

The pacing pellets trigger ELMs when they reach no more than half-way into the H-mode pedestal, and high speed imaging of the pellets shows formation of filaments near the pellet, suggesting that ELMs are triggered by local triggering of the instability and not by increasing the density at the top of the pedestal. The observed penetration of the pellets is in agreement with pellet simulations using the JOREK code used to predict pellet penetration in ITER [9].

Extrapolating both pellet pacing and RMP ELM-control results to ITER with confidence requires understanding the pedestal structure, its temporal and spatial evolution, and the stability limits that lead to the ELM. The EPED model [10] of pedestal structure provides a conceptual and quantitative framework for developing and interpreting ELM-control experiments. New high repetition rate, high-resolution edge Thomson scattering measurements show how the H-mode pedestal evolves during an ELM cycle (fits to the Thomson data shown in figure 5, with the top of the pedestal determined by fitting the data to a modified hyperbolic tangent fit [11], as indicated). Both the pedestal width and pedestal-top pressure grow steadily in time (figure 5(*b*)), moving along a trajectory of constant pressure gradient that matches the calculated kinetic ballooning mode (KBM) stability limit [12]; fluctuation diagnostics show evidence of high frequency modes in this region with characteristics consistent with KBMs [13]. Comparing calculation and measurement, as in figure 5(*b*), we observe that when the evolving pedestal crosses the peeling–ballooning mode pressure limit, an ELM occurs and the cycle repeats. Thus, mechanisms which prevent the pedestal height or width from growing should, in principle, suppress ELMs. However, unravelling the edge plasma response to applied RMPs in ELM-control experiments in order to validate models or improve understanding is challenging due to the steep edge pressure gradients and large magnetic shear in the pedestal region.

Experiments featuring temporal modulation of the $n = 2$ and $n = 3$ RMP toroidal phase and amplitude are providing new insights by comparing changes seen in measurements at different toroidal, poloidal, and radial locations around the tokamak. The data reveal a complex plasma response that includes helical displacements at the edge combined with modulation in the density, temperature, and fluctuation

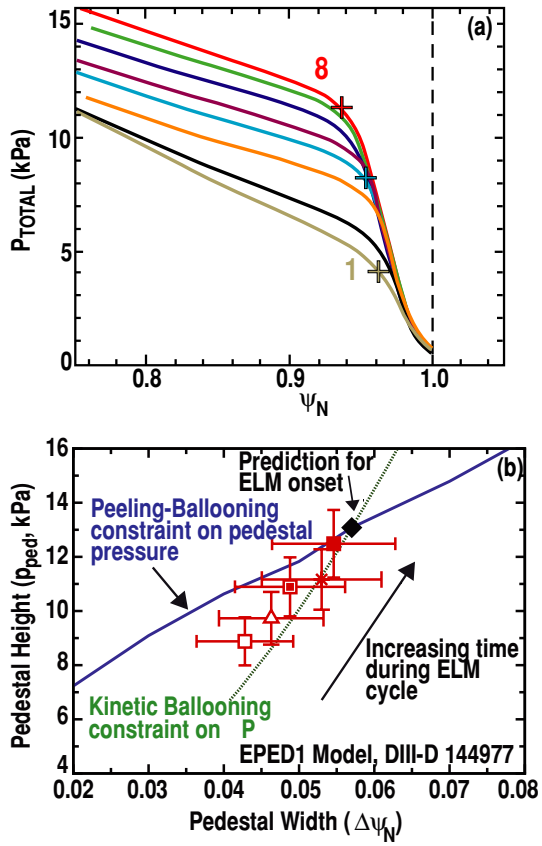

Figure 5. H-mode pedestal evolution between ELMs. (*a*) Plasma pressure profiles derived from Thomson scattering and charge exchange recombination data versus normalized flux (separatrix at $\psi_N = 1.0$) from (1) right after an ELM to (8) just before the next ELM; markers (+) indicate location of peak pedestal pressure for representative profiles. (*b*) Peak pedestal pressure evolution compared to the EPED model.

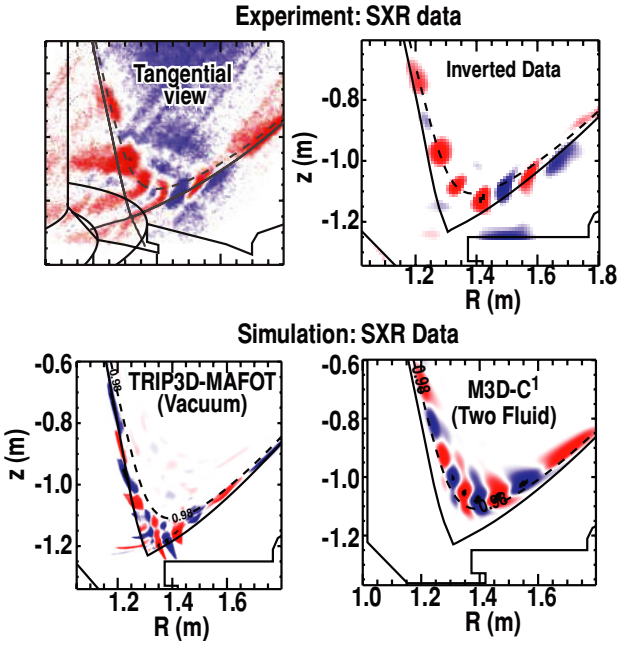

Figure 6. Tangential soft x-ray X-point difference imaging data showing filamentary structure near the X-point arising from $n = 3$ RMP, as compared to simulation. Color intensity indicates magnitude of change in SXR brightness as RMP phase changes by $\pi/3$. Red/blue indicate phase of intensity change ($\pm$) relative to perturbation change. Synthetic diagnostic data from simulation uses model calculated temperature perturbation and assumes uniform carbon concentration.

amplitude near the top of the pedestal where the electron perpendicular drift velocity is zero [6]. New tangential x-point soft x-ray imaging, locked to the RMP toroidal phase modulation shows the existence of filamentary structures or spatial shifts near the separatrix (figure 6), which have been compared to both vacuum-field calculations and two-fluid simulation of the RMP plasma response [14]. The soft x-ray detector has an energy filter which maximizes sensitivity to changes in T_e near the top of the pedestal in the divertor region which occur in phase with changes in RMP phase. Imaging near the x-point provides greater flux-surface resolution due to the large poloidal flux expansion near the field null. As shown, simulations which include two-fluid plasmas response are in better qualitative agreement with measurements than are vacuum-field calculations.

The plasma response in the pedestal region has been examined using a fine-scale scan of the edge safety factor over the range $3.3 \leqslant q_{95} \leqslant 4.0$ which encompasses the typical window of $3.4 \leqslant q_{95} \leqslant 3.55$ for ELM suppression at low triangularity ($\delta \sim 0.26$ instead of $\delta \sim 0.56$ in the ITER-similar shape discharge). The data show [6] the drop in pedestal density with the application of the RMP is nearly independent of q_{95}, while the pedestal T_e (pedestal T_e width) increases (decreases) smoothly as q_{95} decreases across the suppression window, though the T_e pedestal may reach a shallow minimum within the window. Amplitude modulation of the applied RMP shows long-wavelength ($k_\perp \rho_i < 1$) density fluctuations around $r/a \sim 0.9$ increasing rapidly as the RMP amplitude rises, subsequently followed by a drop in the local density, suggesting that RMP changes density by changing turbulent transport [15]. Overall, the full suite of observations is consistent with the picture that the RMP generates a strong resonant response near the top of the pedestal, where the electron drift frequency is near zero ($\omega_{*e} \sim 0$), increasing transport to limit the pedestal width to remain below the peeling–ballooning limit, thereby averting the ELM.

3. Disruption mitigation

Disruptions in ITER are expected to generate large runaway electron (RE) currents compared to present tokamaks (up to 70% of the initial current, or up to 10 MA for a 15 MA ITER discharge) [16]. While massive gas injection (MGI) has been shown to mitigate the effects of the thermal quench, it will be far more challenging to prevent REs by raising density to the so-called 'Rosenbluth density' [17] in ITER. Experiments in DIII-D using either MGI or shattered pellet injection (SPI) have so far obtained <20% of the relevant target value to prevent runaway generation in DIII-D [18, 19], based a calculation of the average toroidal electric field in the RE plasma using magnetics data and a simple circuit model for the plasma self-inductance and interaction with walls and coils [20]. Increasing the impurity injection rate to raise the electron density further has the unwanted drawback of increasing the plasma resistivity and significantly shortening

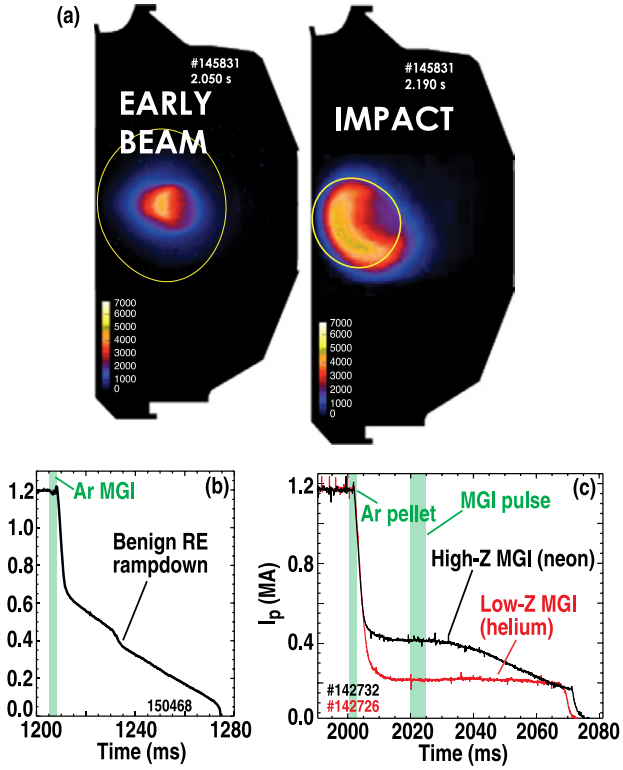

Figure 7. (*a*) Images of synchrotron emission from disruption-induced REs with overlay of limiting current-channel flux surface inferred with EFIT. 140 ms elapsed time when hot core contacts inner wall. (*b*) Plasma current showing enhanced RE dissipation with 113 Pa m^3 argon injection before thermal quench. (*c*) Plasma current traces with neon and helium MGI after thermal quench, showing increased RE dissipation with higher-Z gas.

the duration of the current quench, implying unacceptably high electro-mechanical loads for first-wall components in ITER. Fortunately, high-Z MGI at present assimilation levels can significantly reduce the potential damage from disruption runaways in ITER by dramatically increasing RE dissipation should their current be significant.

Systematic study of RE dynamics and dissipation in DIII-D shows that most high-current ($I_{RE} < 0.6$ MA), high energy (~20 MeV) RE beams limit on the inner wall for several hundred milliseconds, smoothly decaying in size, without significant wall interaction [20]. Similar behaviour is observed for RE beams which drift vertically into the upper or lower divertor surfaces. Figure 7(*a*) shows synchrotron emission for REs in DIII-D formed during the current quench in a disruption triggered by injection of an argon pellet containing 1 Pa m^3 of argon ($N_{Ar} \sim 0.7N_e$) at 2.0 s, with similar injection timing as that of figure 7(*c*). The most energetic RE exist only in the very core of the residual current channel, as determined from images of synchrotron radiation. Strong interaction with the wall does not occur until the inner-wall limited RE current channel contracts to the point where this energetic core (~0.3 m diameter) finally contacts the wall, as evidenced by a sharp rise in carbon radiation and loop voltage. At this point, the beam dissipation rate increases sharply, and though the mean RE energy appears to increase, the total energy is mostly in the poloidal magnetic field at this time; analysis shows most of the residual magnetic energy is then safely converted to a current of low energy electrons which hit the wall without damage. No significant wall damage has been observed even after many such disruptions producing significant RE currents, reflecting both the largely benign termination process and the uniform coverage of the centrepost and divertor regions with graphite tiles in DIII-D.

Massive high-Z impurity gas injection strongly increases the RE dissipation rate, smoothly reducing the current at final termination to less than 10% of the initial RE current, reducing potential for wall damage. Argon or neon injection significantly increase RE dissipation, whether introduced before the disruption shown in figure 7(*b*) or after (following an Ar pellet-induced disruption as shown in figure 7(*c*)) RE formation strongly increases the dissipation rate. In most cases, we observe complete benign dissipation of RE beams (with currents up to 600 kA) without active position control, by which we mean that, even though standard vertical plasma position control for inner-wall limited plasmas remained active through the disruption, the system was not providing significant correction. In these experiments, gas injection ranging from 130 Pa m^3 to 300 Pa m^3 is provided on the low-field side of the plasma at a single location near the top of the plasma (opposite the divertor).

In discharges with active position control consisting of an open-loop outward push by the shaping coils immediately after the current quench followed by vertical position control, the RE beam current ($I_{RE} \leqslant 300$ kA) can be maintained out to the volt-second limit of the ohmic solenoid or until the current is smoothly ramped to zero, allowing precise loop voltage, electric field, impurity spectroscopy, and density measurements under a variety of conditions [21] that enable comparison between measured and predicted dissipation rates. Overall, the dissipation rate is as much as 10× higher than expected from e–e collisions only, and the measured RE energy distribution shows a much larger fraction of lower-energy electrons than expected from avalanche theory and e–e collisions alone [19]. These results suggest that prompt massive injection of high-Z impurity atoms at the current quench, reaching total (bound + free) electron densities well below the Rosenbluth density, may provide a reliable means for safely dissipating large RE currents without damage to internal components in ITER.

Other disruption mitigation studies [20] systematically examined the first-wall heat flux resulting from vertical displacement events (VDEs) in single-null discharges. High speed IR TV measurements (complete divertor profile every 83 μs) showed that most of the heat flux was deposited on the inner wall near the divertor, independent of toroidal field direction; low shot-to-shot variation implies less than 30% toroidal variation, though detailed comparison with magnetic probe data to estimate the effect of low-order modes or other 3D effects has not been carried out. Prompt argon injection at the start of the thermal quench reduced the divertor heat flux by 40%, though little reduction was observed if delayed by 25 ms.

4. Plasma rotation and MHD control in the burning plasma regime

The DIII-D research program places high priority on experiments which simulate planned ITER operating scenarios,

matching shape, β_N, collisionality ($\nu*$), rotation, and stability. Furthermore, due to their large moment of inertia, ITER plasmas will have low externally driven rotation compared to present tokamaks which have significant neutral-beam heating. Plasma rotation in DIII-D can be controlled by varying the mix of co-I_p (15 MW maximum) and counter-I_p (5 MW maximum) NBI torque and power. The scaled ITER equivalent NBI torque ($T^{equiv}_{NB,D3D}$) is defined as that which would produce the same rotation in DIII-D as would NBI torque in ITER ($T_{NB,ITER}$). Assuming $\Omega = T\tau_L/I_{plasma}$ and the angular momentum confinement time (τ_L) varies linearly with the energy confinement time in each tokamak, using the moment of inertia (I_{plasma}) computed from the density profile with transport codes we obtain

$$T^{equiv}_{NB,D3D} = T_{NB,ITER}\frac{I_{D3D}\tau_{E,ITER}}{I_{ITER}\tau_{E,D3D}} \cong 0.3\text{–}1.0\,\mathrm{N\,m}, \qquad (1)$$

depending on discharge conditions. Further details are provided in the appendix of [22].

The importance of external NBI torque and resulting rotation is illustrated by the sensitivity of low-torque discharges to tearing modes, which reduce confinement and can lock to low-n field errors to produce a disruption. With strong co-current NBI (total NBI torque ~2.9 N m), and feedback controlled $\beta_N \sim 2$, ITER-shaped plasmas at $I/aB = 1.4$ reached and maintained stationary conditions with $H_{98y2} > 1$, $l_i \sim 0.8$–0.9, and free of tearing modes for $>10\tau_R$ [23]. However, small changes in β_N (particularly a reduction of ~10%) or a small reduction in co-current NBI torque and plasma rotation resulted in increased tearing mode activity. Adding ~3 MW of ECCD broadly deposited near the $q = 3/2$ surface (~30 kA total current drive) suppressed the tearing modes even as the NBI torque was reduced to the scaled ITER equivalent of <1 N m by adding 1.8 MW of counter-injection on top of the 2.6 MW of co-injected neutral-beam power, allowing stationary conditions to be maintained for more than four resistive times [24] (figure 8). Subsequently, long-pulse ITER baseline scenario demonstration discharges featuring low-torque start up and ramp up were obtained.

Successful low-torque ramp up to stationary conditions simulating the ITER hybrid or advanced inductive (AI) scenario, has been demonstrated [23]. This scenario features higher $\beta = 3.1$ operation with improved stability at higher $q_{95} = 4$ (i.e. lower current) than the ITER baseline case. Equivalent stationary conditions were obtained by either ramping up β_N at constant torque following low-torque start up or by ramping down torque and rotation at constant β_N after start up with significant NBI torque. Reducing the NBI torque and plasma rotation reduced energy confinement significantly (H_{98y2} dropped from 1.5 typical of our best AI plasmas to 1.0) in either case. Once stationary, these discharges operated at $\beta_N \sim 3$, $H_{98y2} \sim 1$, $q_{95} \sim 4$, obtaining equivalent fusion gain $G = \beta_N H_{89}/q^2_{95} \sim 0.35$, nearing that expected for ITER $Q = 10$ operation ($G = 0.4$). Similar to the ITER baseline scenario experiments described above, at reduced torque the plasma becomes more susceptible to neoclassical tearing modes (NTMs) which generally slow plasma rotation causing a locked mode. Application of ~1 MW of ECCD or electron cyclotron heating (ECH) near or even inside the $q = 2$ surface suppressed these modes, allowing stable high

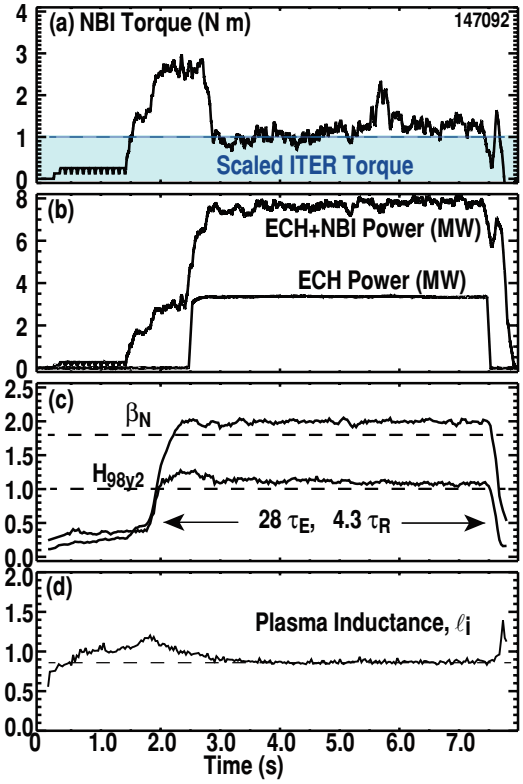

Figure 8. Low-torque ITER simulation discharge (scenario 1) with low rotation. (*a*) Neural beam torque, with the shaded region indicating the range of ITER equivalent torque, (*b*) total injected and ECH power (1.8 MW counter-NBI and 2.6 MW co-NBI), (*c*) β_N and H-mode confinement factor H_{98y2}, (*d*) plasma inductance l_i.

performance operation ($\beta_N \sim 2.5$) even with zero net NBI torque and very low plasma rotation (~1 kHz).

Research continued on developing the physics basis for another promising ITER operating mode, the ELM-free QH-mode [5]. Recent experiments using only external coils (outside the toroidal field coils) have produced stationary QH-mode discharges with low plasma rotation, extending the operating space to include co-current NBI torque providing 3–4 times the torque scaled from the ITER beams [25]. The strong edge rotational shear needed for QH-mode access was maintained using counter-I_p torque arising from neoclassical toroidal viscosity (NTV) [26] produced by applying non-resonant magnetic fields (NRMF). Best results have been obtained with $n = 3$ external coils, though $n = 3$ NRMF using internal coils also works well.

These QH-mode plasmas exhibit excellent confinement at low rotation with low NBI torque ($H_{98y2} = 1.3$), as shown in figure 9, and in contrast to conventional ELMing H-modes at low rotation. QH-mode discharges operate stably to at least $\beta_N = 2.9$, though no systematic study of the beta limit has been carried out. Discharges such as the one in figure 9 have low pedestal collisionality $\nu^*_{ped} = 0.05$ at $q_{95} = 4.7 (I/aB = 1.05)$ with nearly zero core rotation [27]. Higher current discharges with $G = 0.4$ have been obtained at $q_{95} = 3.4$ as well. No systematic study of the beta limit for QH-mode has been carried out, though upper-single discharges have reached $\beta_N \sim 2$. The fact that QH-mode can be obtained robustly over a wide range in heating power using NRMF to produce the

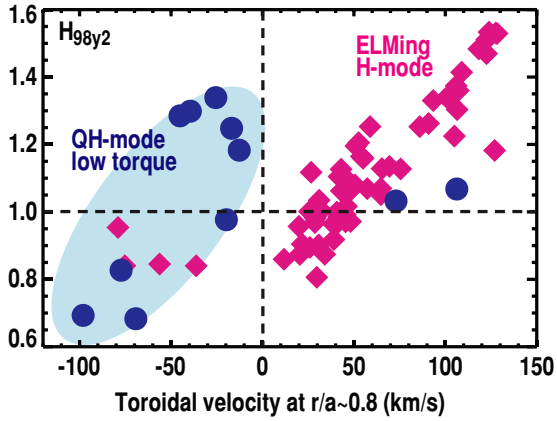

Figure 9. ELM-free QH-mode (solid circles) and ELMing H-mode (solid diamonds) confinement factor versus edge ($r/a = 0.8$) toroidal rotation velocity.

rotational edge shear may make it an attractive operating mode for ITER.

ITER may be susceptible to tearing modes if the plasma rotation is small or fast-ion-stabilized sawteeth grow to large amplitude during the fusion burn. Therefore, ITER plans to have active NTM control.

Improved NTM control integrating all the elements of NTM control for ITER is now available on DIII-D. Actively tracking the $q = 2$ and/or $q = 3/2$ surfaces and promptly applying ECCD when NTMs are first detected reduces the power required to suppress tearing modes, confirming the feasibility and benefit for such feedback control in ITER. Several integrated control schemes have been developed and tested, which combine real-time motional Stark effect (MSE) measurements to locate the target q-surface, fast steering mirrors on the EC launchers to adjust the deposition location, a model-based aiming algorithm which corrects for beam diffraction in the plasma [28], and reliable methods to detect the NTM. Both $3/2$ and $2/1$ NTMs have been suppressed ($2/1$ suppression shown in figure 10), with significantly more power required to suppress the $2/1$ mode than the $3/2$ mode (2.9 MW versus 0.6 MW), as expected from its larger growth rate and the requirement that the EC driven current must be greater than the missing local bootstrap current at the mode-rational surface [29, 30]. Suppression of $2/1$ NTMs required prompt application of ECCD at the $q = 2$ surface following mode detection, otherwise the mode would lock before it saturated and cause a loss of H-mode confinement. Prompt application of ECCD at the $q = 3/2$ surface yields a 60% reduction in the minimum power required for suppression (to 0.6 MW) as compared to applying ECCD after the mode has saturated. In extreme cases where the tearing mode grows large enough to lock, experiments have shown that 3D field coils can be used to align the toroidal location of the O-point with ECCD deposition to stabilize the mode and avoid disruption [31].

Large sawteeth can destabilize tearing modes and cause disruptions. We have carried out experiments to stabilize or reduce the size of fast-ion stabilized sawteeth in DIII-D. In ELMing H-mode discharges, ECCD was used to increase the magnetic shear near the $q = 1$ surface and reduce the size of fast-ion stabilized sawteeth oscillations, thereby allowing operation at $\beta_N > 3$ without large 2/1 tearing modes [32], an

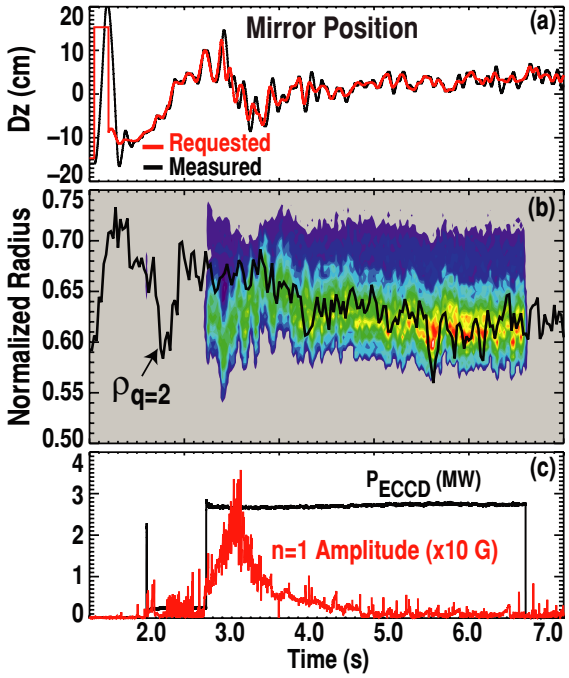

Figure 10. Neoclassical tearing mode control showing time traces of (a) launcher mirror position tracking requested position, (b) location of $q = 2$ surface superimposed on colorized ECCD intensity plot as derived from ONETWO profile analysis and EC ray tracing, (c) ECCD power and 2/1 tearing mode amplitude from edge magnetic probes.

important demonstration of the physics basis for this approach in ITER.

EFC experiments utilizing large proxy $n = 1$ error fields from either external coils or an ITER test blanket module (TBM) mock-up coil [34, 35] show that correcting only the lowest-order error field components can introduce strong residual rotational drag which reduces stability and confinement. The TBM mock-up coil introduced a highly localized field perturbation at a single toroidal location, while the external C-coils (figure 11(a)) created a more purely $n = 1$ error field without higher order harmonics. Two toroidal rows of six internal coils (the I-coils) provided the $n = 1$ EFC in each case [36]. In the TBM experiments, the change in toroidal rotation of the plasma with constant neutral-beam torque was used to infer the change in drag on the plasma rotation caused by the TBM error field with and without EFC; application of $n = 1$ EFC using the I-coils reduced the drag due to the TBM error fields by only 25% [37]. In the C-coil error field experiment, the effect of EFC was determined by its impact on the low density locked-mode threshold; only modest improvement was observed when using $n = 1$ EFC to correct the $n = 1$ error field. Modelling with the IPEC perturbed MHD equilibrium code [38] explained the results for this $n = 1$ proxy error field experiment [39] through an increase in non-resonant fields and rotation braking when the low-order resonant correction was applied (figure 11(b)). The figure shows the flux-surface average neoclassical drag torque on the plasma due to non-resonant field components produced separately by the proxy error field (black trace) and by the I-coil used to correct the $n = 1$ error field (red trace). So even though the applied ERC reduces the $2/1$ resonant field, it

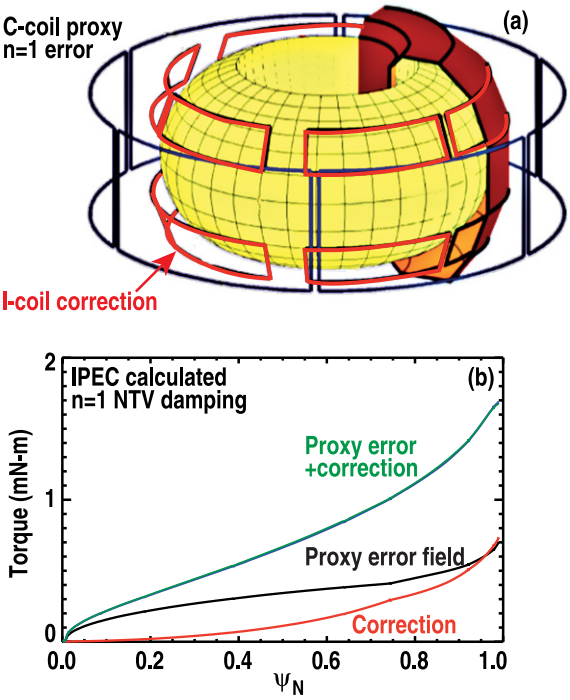

Figure 11. EFC experiments using (*a*) external C-coil to produce the $n = 1$ error field and internal I-coils to provide correction. (*b*) Neoclassical rotational damping torque for the proxy error field, correction coils and combined proxy error and correction coils.

actually increases the total drag from non-resonant components significantly [36], as shown by the green trace.

These results confirm present understanding that EFC strategies must include the full plasma response of all the field components to determine the best coil combinations for correction [39]. This suggests that optimal correction may require ITER to maintain flexibility in its EFC coil set to produce multiple poloidal harmonics, possibly including its ELM-control coils in the mix while using measured plasma rotation to provide feedback control for optimizing the correction.

During the TBM error field experiments, hot spots on the protective tiles covering the TBM mock-up module associated with NBI were observed using infrared thermography. The location of the hot spots and the calculated surface heat flux were compared with predictions from four different orbit-following simulation codes (ASCOT [40], SPIRAL [41], OFMC [42] and DELTA5D [43]) for cases with a wide variety of energetic particle sources (co-, counter-, and on-off axis NBI). Results show that vacuum-field calculations are sufficient to calculate the EP losses produced by the localized error fields and that plasma response plays at most, only a minor role in prompt loss of these fast ions [44].

5. Developing predictive capability for burning plasma experiments

It is important to develop validated predictive models for ITER to guide design choices, help determine operational requirements, and inform experimental planning once ITER is operational. Informed planning will enable most efficient use of the facility and maximize progress towards fusion energy. Fusion gain depends on the global energy confinement, which in H-mode is determined by the combined effects of stability and transport in the core and edge-pedestal regions. Validated transport models are needed for both and have been the subject of recent joint experiments involving DIII-D, NSTX, and Alcator C-Mod [45, 46].

The DIII-D program carried out experiments to measure core transport stiffness in L-mode and H-mode discharges, and to further explore the theory-measurement discrepancy in L-mode edge transport at $\rho \geqslant 0.7$. Stiffness refers to a sharp increase in transport when the temperature gradient exceeds a critical value; high stiffness in H-mode implies that the core profile simply rides on top of the pedestal, yielding $P_{\rm fusion} \propto \beta^2_{\rm pedestal}$. It is important to examine transport and stiffness in L-mode as well as H-mode, because L-mode transport impacts both the plasma current profile and stability (via the $T_{\rm e}$ profile) during the initial $I_{\rm p}$ ramp, and L-mode transport determines the edge turbulence and shear that governs the power requirements for achieving H-mode access.

The critical-gradient scale length for the onset of increased electron transport in L-mode discharges was measured using localized ECH to vary the gradient scale lengths at the plasma mid-radius by over factor of 4 while changing the local heat flux in small steps by a factor of 10, as shown in figure 12. Measurements were obtained with and without co-, counter- and balanced-$I_{\rm p}$ NBI heating. Both power balance and heat pulse propagation showed similar responses, consistent with a sharp rise in transport when the gradient scale length $1/L_{T_{\rm e}} = \nabla T_{\rm e}/T_{\rm e} > 3.0\,{\rm m}^{-1}$ [47, 48] (figure 12(*b*)). During these experiments, a sharp rise in local electron temperature fluctuations and a change in the $\tilde{n}\tilde{T}_{\rm e}$ cross-phase co-incident with the change in transport was observed for the first time (figure 12(*c*)), using correlation electron cyclotron radiometry [49].

The sharp rise in $T_{\rm e}$ fluctuations indicates that trapped electron modes are becoming important, providing an excellent test for gyrokinetic simulations. Simulations using both the gyro-Landau fluid model TGLF [50] and the nonlinear gyrokinetic microturbulence code GYRO [51] show the sharp rise in thermal transport, $Q_{\rm e}$, above the critical gradient (figure 12(*b*)) though the electron heat flux in GYRO appears to saturate at much lower value than either experiment or TGLF [46]. GYRO shows the $T_{\rm e}$ fluctuations should increase with higher gradients although the fluctuation levels are lower than observed in this experiment.

In separate beam-heated H-mode discharges, no sign of a critical-gradient threshold for increased ion or electron transport is observed, possibly because low values of ∇T could not be accessed. These experiments examined both co-$I_{\rm p}$ and balanced NBI heating, varying beam power by a factor of three (3.3–9.2 MW). The discharges were designed to minimize changes in the plasma parameters in the region $\rho \geqslant 0.8$ by operating at low triangularity, this producing discharges with rapid ELMs where the pedestal remains close to the peeling–ballooning limit. In fact, the ion and electron temperatures in this region between $\rho = 0.8$ and the pedestal rose somewhat with increasing heating power, in contrast to the assumption of fixed pressure at $\rho = 0.8$ used as a boundary condition in many core transport simulations. The results of the experiment

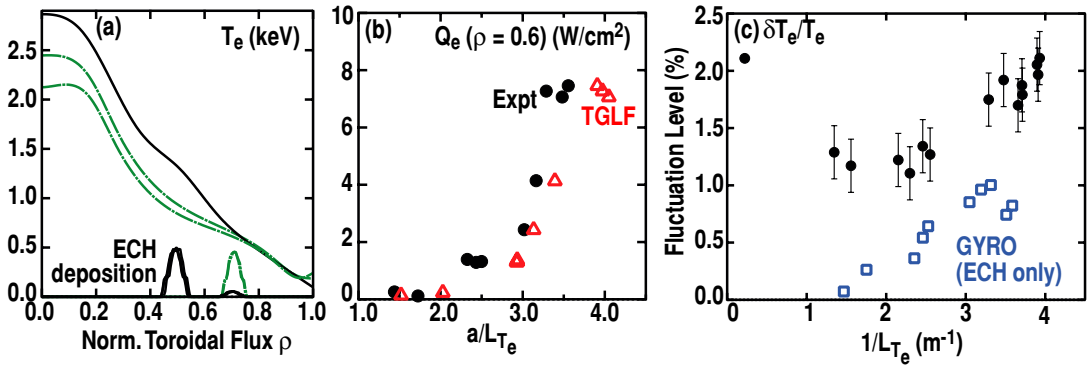

Figure 12. L-mode critical-gradient electron stiffness in DIII-D. (*a*) Change in ECH location and resulting change in electron temperature profile. (*b*) Resulting change in electron heat flux at $\rho = 0.6$. (*c*) Resulting electron temperature fluctuations at $\rho = 0.5$. TGLF simulation (triangle), GYRO simulation (square) results in (*b*) and (*c*).

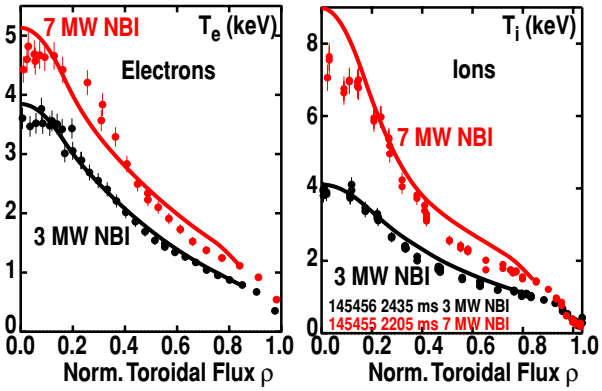

Figure 13. Measured H-mode ion and electron temperature profiles versus TGLF simulation predictions using measured T_e and T_i at $\rho = 0.85$ as boundary condition. 3 MW NBI heating (black); 7 MW NBI heating (red). TGLF simulations (solid line).

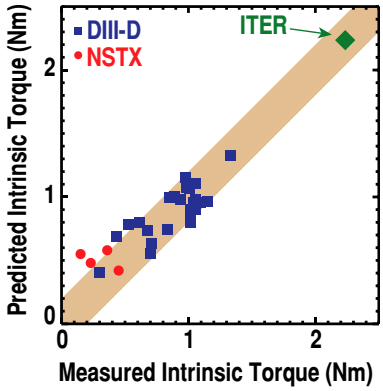

Figure 14. Predicted versus measured intrinsic torque for H-mode plasmas, with the prediction for ITER using the same methodology as in [19].

show that, inside $\rho \sim 0.5$, electron thermal transport is stiffer than ion, while at larger ρ the stiffness is similar (figure 13), in agreement with both TGLF and full gyrokinetic simulations (solid lines) using the measured pedestal parameters at $\psi_N = 0.85$ [45] as the boundary conditions.

Gyrokinetic turbulence/transport simulations in DIII-D often show good agreement with experiment in the core of L-mode plasmas inside $\rho \sim 0.5$, but under-predict both the thermal transport and fluctuation levels (i.e. have a 'transport shortfall') towards the edge, $\rho > 0.75$ [52, 53]. The shortfall is observed in codes using either PIC or continuum solvers [54]. Taken together, these results point to a discrepancy at a fundamental level. Recent L-mode transport experiments examined the dependence of the shortfall on the safety factor q_{95}, finding that the transport shortfall increased in magnitude and spread further inward towards the core as q_{95} increased [55]. Turbulence measurements using beam emission spectroscopy (BES) and a new correlation electron cyclotron emission (ECE) diagnostic show density and electron temperature fluctuation levels in the outer region of the plasma also increasing with q_{95}. The increased transport shortfall with rising fluctuation levels is consistent with a hypothesis that the gyrokinetic approach to transport may fail at high fluctuation levels [56].

Core transport and stability are strongly affected by plasma rotation and rotational shear, which must be included in transport models. It is straightforward to calculate the torque on the plasma from NBI, but the intrinsic torque arising from neoclassical and other transport effects is not well documented. Using co- and counter-NBI to apply a step change in NBI torque, the intrinsic torque as a function of radius has been inferred from the changes in the rotation profile, and from these data a simple physics-based model of intrinsic rotation has been developed. In the edge-pedestal region, data show that turbulent Reynolds stress alone is insufficient to explain the formation of a large intrinsic edge rotation layer. A model which includes edge thermal-ion orbit loss ($\propto \sqrt{T_i}$) and ∇P_{ped} describes measured intrinsic edge torque in DIII-D and NSTX H-mode plasmas quite well [57], including AI discharges which exhibit higher intrinsic torque reaching 1.5 N m (figure 14), as compared to the 4–5 N m neutral-beam torque for typical AI discharges at moderate $\beta_N \sim 2.7$ with only co-current NBI. As shown, this model predicts an intrinsic torque of ~2 N m in ITER, compared to 35 N m provided by the neutral beams, implying that rotation in ITER will be determined largely by the applied neutral-beam torque.

The study of plasma rotation and transport benefits from first-time simultaneous measurements of main-ion and impurity ion (carbon) rotation profiles. With low external torque, flow shear will largely depend on ∇P and poloidal flow velocity. The new measurements [58, 59] show anomalously large main-ion poloidal rotation in the ion-diamagnetic direction at low collisionality ($\nu* < 0.1$) in low-torque

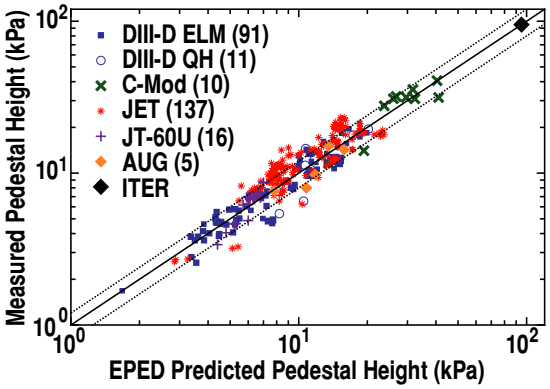

Figure 15. Measured pedestal height versus predicted pedestal height from the EPED model for 270 tokamak discharges from five tokamaks as shown. Predicted pedestal height for ITER (diamond symbol at upper right) agrees with design target value for $Q = 10$ operation.

H-mode discharges, as compared to the usual inference of main-ion flow velocity from charge exchange recombination measurements of carbon. These results may have implications for core transport in ITER, where the toroidal rotation contribution to the radial electric field may be small. Poloidal rotation that is anomalously large in the ion-diamagnetic direction provides a larger (more positive) radial electric field, and radial electric field shear. A scaling of main-ion poloidal flow was applied to ITER conditions using TGYO-TGLF modelling, and resulted in increased core $E \times B$ shear rate that approached or exceeded the local long-wavelength turbulence growth rates [60]. Enhanced $E \times B$ flow shear in the simulations from anomalous poloidal rotation was seen to reduce the ion thermal transport and produce an increase in central ion temperature on the order of 10%.

The relatively good agreement between TGLF transport simulations and H-mode data relied in part on using the measured pedestal parameters as a boundary condition for the core plasma. So predicting the temperature at the top of the pedestal is a key element in building a robust scientific basis for the H-mode confinement database used to predict performance in ITER [61]. Coordinated experiments involving DIII-D, C-Mod, and NSTX produced high-resolution edge-pedestal profile data which were compared against a number of theory-based simulation codes [45]. Adding the data from C-Mod doubled the range over which the EPED model correctly predicts the pedestal height without recourse to adjustable or fitted parameters. With the present database growing to 270 discharges from 5 tokamaks (figure 15), there is increased confidence that the EPED model can be used to predict the pedestal pressure height in ITER to within ~20%, using MHD and kinetic stability calculations and incorporating no fitted parameters. Significantly, the predicted value matches the expectation for achieving $Q = 10$ H-mode operation in ITER. This model also guides ELM mitigation experiments with RMPs and pellets, and is consistent with interpretation of ELM-free QH-mode operation.

Obtaining the benefit of H-mode confinement naturally requires H-mode access. However, the trigger for the L–H transition has remained elusive even though the paradigm of flow-shear stabilization of edge turbulence following the

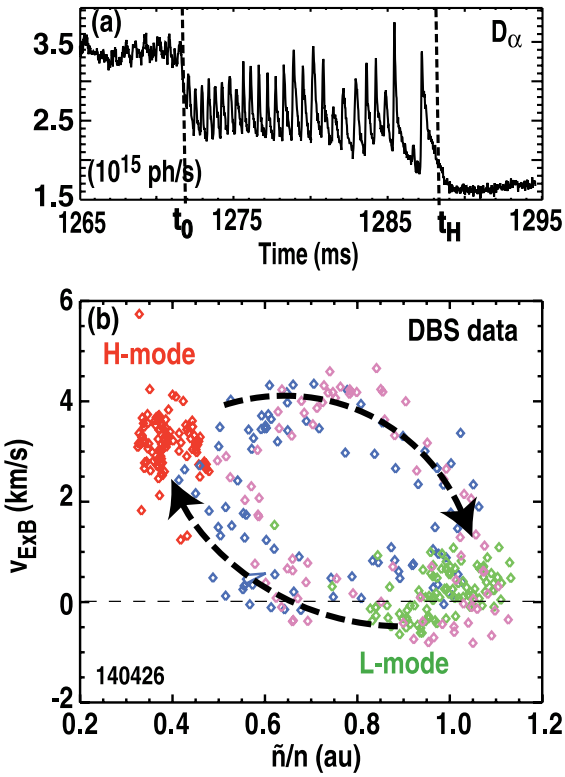

Figure 16. Limit-cycle oscillations during a 'dithering' H-mode transition. (*a*) Divertor H_α brightness showing oscillations starting from L-mode at 1272 ms and ending with steady H-mode at 1289 ms. (*b*) Microwave DBS data for $k_\theta \rho_s \sim 0.5$ measured between 1 and 2 cm inside the separatrix. Red and green indicate H-mode and L-mode data, respectively. Blue and green data from two neighbouring channels during the limit cycle.

H-mode transition is well documented. Recent diagnostic developments have provided significantly improved temporal resolution for turbulence and turbulent flow measurements that are revealing the underlying physics of the transition threshold [62]; see also [63, 64].

In DIII-D, near the H-mode power threshold, so-called 'dithering' H-mode transitions exhibit limit-cycle oscillations are observed, which allow study of the transition dynamics on an expanded timescale, as illustrated by the variation in H_α emission shown in figure 16(*a*) when the plasma transitions from L-mode to H-mode confinement. Microwave DBS measures both the amplitude of high frequency density fluctuations and $E \times B$ flow ($v_{E\times B}$) near a region around the separatrix with high temporal resolution. DBS data from a 3 ms time interval during the limit cycle phase, shown in figure 16(*b*) illustrate the predator-prey dynamics going from high $\tilde{n}/n$ and low $v_{E\times B}$ and back again; eventually the pressure-gradient driven flow shear locks in the H-mode with high flow shear and low fluctuations [65, 66].

BES measurements across the L–H transition show trends in turbulence and turbulent flows at the H-mode transition that mirror well-known density and magnetic field scaling of the H-mode power threshold [67]. Just prior to the transition, the data show reduced high frequency (20–150 kHz) fluctuation amplitudes near the separatrix at higher toroidal field, suggesting a reduced drive for zonal flows, while BES velocimetry measurements show low frequency turbulent flow

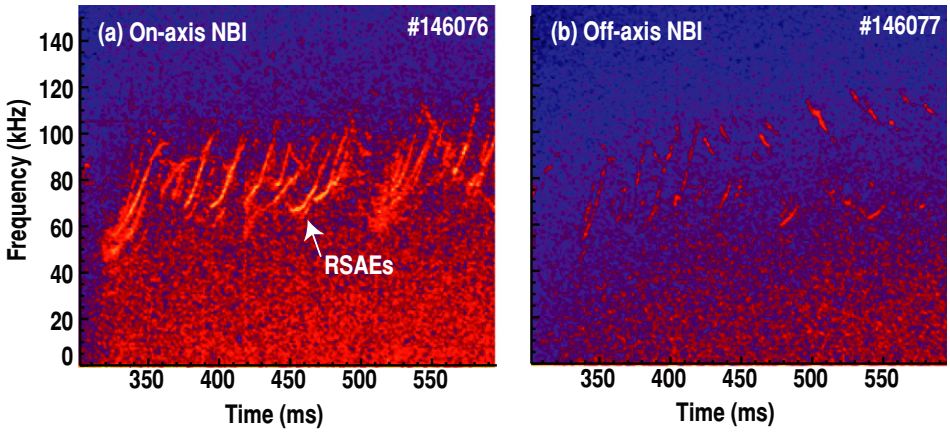

Figure 17. Cross power of adjacent ECE channels that are located near $q_{\min}$ (at $R \cong 195$ cm) showing RSAE activity during (a) on-axis and (b) off-axis injection. The same logarithmic color scale is used in both figures. In the off-axis case, mode activity after 400 ms coincides with brief on-axis beam pulses for diagnostic purposes.

velocity shear increasing at lower density. Both trends are consistent with the observed scaling in H-mode power threshold ($P_{\rm LH} \propto n^{0.7} B^{0.8}$). DIII-D H-mode transition data have also been incorporated into an updated multi-machine database [68].

Fast-ion transport is a key element to achieving fusion gain. Off-axis injection of neutral beams into DIII-D has provided new insights into fast-ion instabilities that may impact alpha-particle and neutral-beam confinement in ITER. Off-axis injection alters the stability of reversed shear Alfvén eigenmodes (RSAE), as shown in figure 17. RSAEs are fast-ion driven instabilities that are localized near the minimum of the q profile (at $\rho_{\rm qmin}$). The enhanced stability for off-axis injection is attributed to flattening of the fast-ion gradient $\nabla\beta_{\rm f}$ that drives the modes unstable. Beam deposition for the off-axis beams peaks near $\rho_{\rm qmin}$ so switching between on-axis sources that inject at the midplane and off-axis sources that aim below the midplane has a large local effect on $\nabla\beta_{\rm f}$, as indicted by the lack of RSAE modes in figure 17(b). At larger minor radius, the fast-ion gradient is similar for on- and off-axis injection, and as a result, switching the angle of injection has little effect on the stability of toroidal Alfvén eigenmodes (TAE) that appear in the outer portion of the plasma [69, 70].

6. Research on the path to fusion energy: high-β steady-state operation

Significant capability for off-axis current drive has been added to DIII-D in order to evaluate advanced configurations having broad current and pressure profiles capable of high $\beta_{\rm N}$ fully noninductive steady-state tokamak operation [71]. Theory and experiment indicate that broad current profiles peaked off-axis are beneficial for steady-state high performance solutions. This line of research supports both the ITER steady-state mission and future tokamak development.

Successful modification of a DIII-D neutral-beam line now provides capability for up to 5 MW of adjustable off-axis co-current NBI (OANBI) out of 20 MW maximum total NBI power. The adjustment is accomplished [72] by tilting the back end of the beam line vertically upward about a pivot point located in the beam line vacuum vessel entrance at the plasma midplane. The NBI poloidal tangency radius for the centreline of the beam is adjustable during a single experimental day over the range $0 \leqslant \rho \leqslant 0.5$ for beamline tilt angles of $0 \leqslant \theta \leqslant 16.5^\circ$ for full-size elongated plasmas ($a \sim 0.62$m, $\kappa_{95} \sim 1.8$). The grid structures and collimating apertures for the two sources in the beam line were modified to reduce interaction with the sides of the tokamak entrance port. The aiming and positioning of the neutral beams was checked at the start of tokamak operation using H_α visible imaging and beam-dump heat flux measurements [73], as shown in figure 18(a). Measurements comparing D–D neutron production, fast-ion profiles, and plasma heating indicate that, compared to unmodified beams operating at similar parameters, the source and beam line modifications have reduced the beam power reaching the plasma by ~15–20%, independent of the beam line tilt angle; the source of the reduced injection power is still being studied.

Comprehensive measurements show that off-axis neutral-beam current drive and fast-ion transport agree with numerical simulation [74]. The neutral-beam current drive is very sensitive to toroidal field direction, which significantly changes the ratio of trapped to passing particles; 'reversed' $B_{\rm T}$ ($I_{\rm p}$ and $B_{\rm T}$ in the same direction) provides 45% more current drive and peaks the current further off axis. Figure 18(a) shows the NBI current drive due to off-axis injection as compared on-axis injection as derived from MSE-constrained equilibrium reconstruction; there is good agreement in shape and magnitude with NUBEAM Monte Carlo beam ionization simulation [75] in these low-β discharges. More extensive studies show no degradation in current drive due to microinstabilities as β increases [74].

The off-axis current drive capabilities enable access to a new range of profiles with sustained minimum safety factors $q_{\min} > 2$, for durations greater than 2 s [76], as shown in figure 19. These high-$q_{\min}$ plasmas operating at $B_{\rm tor} = 1.8$ T maintain $\beta_{\rm N} \sim 3$, well below the calculated beta limit ($\beta_{\rm N} > 4$). Because $q_{\min} > 2$, there are no deleterious 2/1 and 3/2 tearing modes, although higher order modes do appear, often as q passes through a rational value; if such modes persist, they reduce confinement by ~15%. These discharges using off-axis injection are not limited by stability, but rather by available heating power and reduced confinement. Because

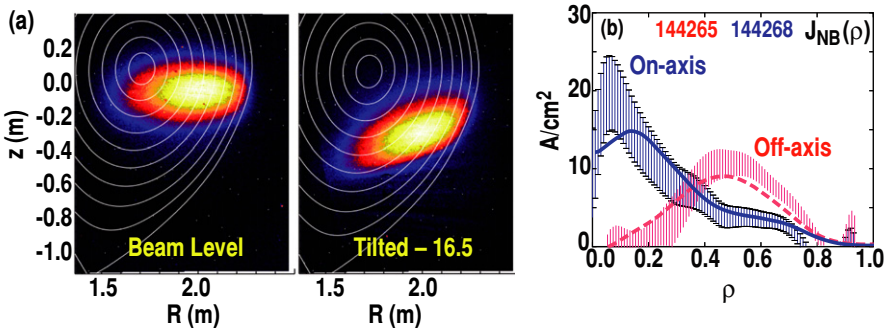

Figure 18. Off-axis NBI on DIII-D. (*a*) NUBEAM calculation showing starting location for fast ions created from beam-injected neutrals for on-axis and fully-tilted 16.5 deg off-axis injection. Path curvature results from projection of tangential beam path onto the cross section. (*b*) Toroidal current density from neutral-beam injection, derived using Ohm's law and the time evolution of magnetic flux profile with error bars as indicated. Solid lines show NUBEAM predictions.

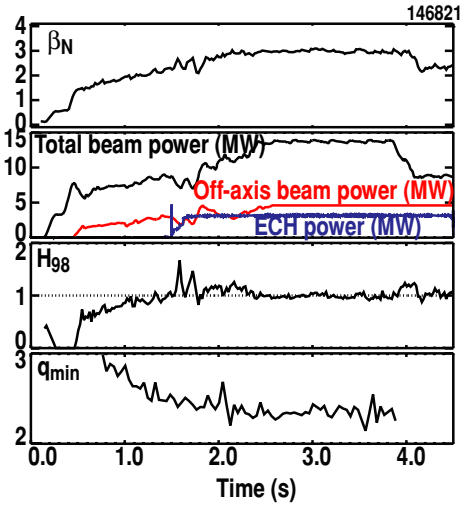

Figure 19. Stationary high β_N, high q_{min} discharges maintained with off-axis NBI and ECCD.

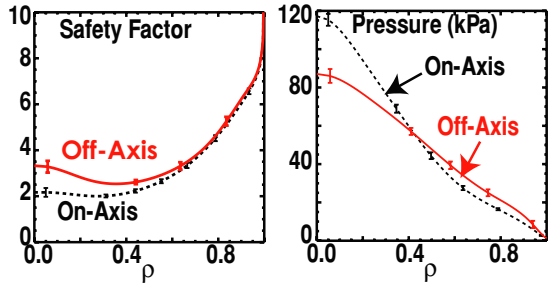

Figure 20. Current and pressure profiles for steady-state discharges with off-axis NBI compared to previous results with on-axis NBI only.

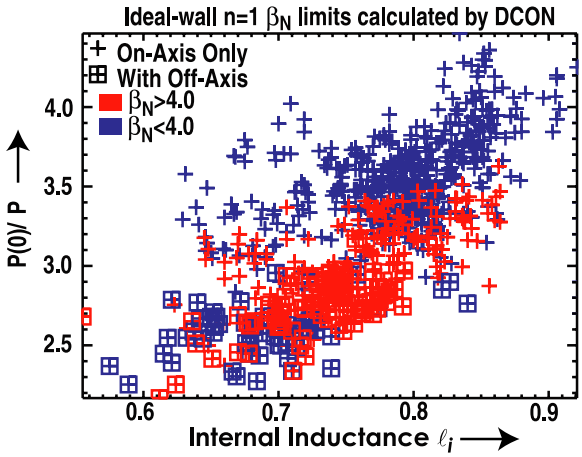

Figure 21. Ideal-wall $n = 1\beta_N$ limits calculated by DCON for AT discharges with both off-axis (+filled boxes) and on-axis NBI (+only) as a function of pressure peaking and internal inductance. Red symbols have β_N limit >4 and blue have β_N limit <4.

we are seeking to maximize the non-inductive current fraction in our steady-state research, we do not use counter NBI, which limits the input power to ∼15 MW. In addition, although H_{98y2} is still $\gtrsim$1, this value is typically ∼20% lower than comparable discharges with on-axis injection and lower q_{min}. Measurements showing increased Alfvén mode activity in these discharges suggest that increased fast-ion losses might be a contributing factor to reduced confinement, which would be consistent with the observation that H_{89P} does not show a similar decrease (H_{89P} does not correct for the expected fast-ion content in the plasma as does H_{98y2}).

Off-axis injection produces both broader current profiles (lower l_i) and broader pressure profiles ($P(0)/\langle P\rangle \leqslant 3$) than previously sustainable [76], as in figure 20. Both factors should produce significantly higher ideal stability limits than previously obtainable under stationary conditions; DCON [77, 78] calculations of the ideal-wall $n = 1\beta_N$ limit carried out using measured current and pressure profiles show that off-axis injection does produce discharges with higher calculated beta limits than does on-axis injection (figure 21). Discharges with profiles having calculated β_N limits >4.0, indicated by the red symbols in the figure, are most commonly obtained with off-axis injection (box + symbols), in contrast to discharges with on-axis injection (+symbols only) which generally yield calculated β_N limits <4.0 (blue symbols).

Relaxing q_{min} to 1.5 leads to steady-state discharges with improved confinement at $\beta_N = 3.5$ that are close to meeting the predicted requirements for steady-state $Q = 5$ operation in ITER [79] and also for FNSF-AT operating at $Q \sim 4$ [80]. The DIII-D discharges have high non-inductive current fractions, $f_{NI} \sim 0.7$, and are maintained free of low-order tearing modes by OANBI and ECCD for two current profile relaxation times

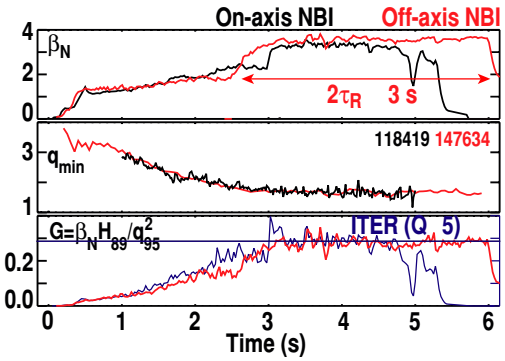

Figure 22. Stationary high β_N H-mode discharges with $q_{min} \sim 1.5$ maintained for $2\tau_R$ with off-axis NBI and ECCD. Typical discharge with on-axis NBI (118419); recent discharge with off-axis NBI (147634). Minimum safety factor generally near $\rho \sim 0.4$–0.5. Without sufficient off-axis current drive, the $n = 1$ tearing mode grows and ends discharge 118419.

($2\tau_R = 3$ s), limited by available beam energy (power and pulse length), as shown in figure 22. The ECCD (3.2 MW) was applied steadily at $\rho \sim 0.4$ and dynamic EFC was also used. The safety factor (both q_{min} and ρ_{qmin}) and pressure profiles generally agree with FASTRAN/ONETWO fixed boundary 1.5 transport simulations [76, 79] that incorporate TGLF transport simulations and realistic heating and current drive inputs. Modest differences that are observed between simulation and experiment in $T_e(0)$ (20% higher than measured) and in the mid-radius T_i profile (steeper computed ∇T_i across $\rho \sim 0.2$–0.3) can be reduced by increasing the fast-ion diffusion coefficient in the core, possibly due to the increased Alfvén eigenmode activity at higher q_{min} noted earlier.

High-β steady-state operation will rely upon and benefit from model-based control algorithms incorporating multiple actuators to produce and maintain optimal q-profiles. Recent experiments on DIII-D have successfully demonstrated this control approach (also planned for use in ITER) by regulating the mix of on- and off-axis co-current NBI power, counter-current on-axis NBI power, off-axis ECCD power, applied OH loop voltage, and line-averaged density. One set of experiments used control algorithms incorporating using data-driven models [81], while the other used algorithms based on first-principles physics models [82]. Both approaches successfully produced and maintained target AT poloidal flux profiles with peak $\beta_N \sim 2.5$ that were significantly different from the naturally evolving profiles using conventional DIII-D feedback control algorithms. The model-based controllers operated robustly across a wide range of plasma regimes, including most of the ramp up phase and the entire flattop phase.

7. Research on the path to fusion energy: integrated core-boundary solutions

Future steady-state fusion devices will place higher demands on plasma facing components (PFCs), and new integrated core-edge-divertor solutions will be needed. Initial integration experiments [76] have used neon injection to enhance edge and divertor radiation in the high β_N steady-state discharges described in section 7. Neon injection in the divertor of these

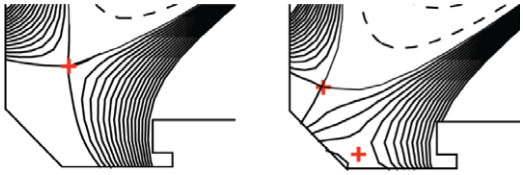

Figure 23. Conventional (left) versus Snowflake-minus [56] divertor configuration (right) in DIII-D.

AT discharges ($\beta_N = 3$ and $q_{min} = 1.5$) doubled the radiative loss from the edge ($\rho \geqslant 0.85$) and divertor without degrading confinement ($H_{98y2} = 1.1$), reaching 50–55% total radiative loss and reducing peak divertor heat flux by ~40% without detachment or formation of an x-point MARFE. Eventually, steady neon puffing and increasing radiative loss caused a reduction in confinement and beta, so future experiments will utilize divertor pumping and feedback control to limit the neon content and total radiative loss to maintain good confinement.

Very promising results were obtained using the snowflake (SF) divertor configuration to reduce the peak heat flux as compared to a standard single-null divertor. Using only the external poloidal field coils, SF divertor configurations [83], such as the Snowflake-minus in DIII-D (figure 23) can provide much larger SOL volume near the X-point, larger divertor contact area in the SOL adjacent to the separatrix (3–4×), and longer parallel connection length than a standard divertor, especially below the X-point, where the plasma, neutral gas, and impurity densities are high. The Snowflake-minus configuration shown in figure 23 has two null points, with the one near the outer divertor target producing very large local flux expansion. Data from an ELMing H-mode discharge, figure 24, show that the increased flux expansion lowers the peak divertor heat flux by about a factor of three. Preliminary analysis of a limited number of SF-minus discharges indicates that the energy loss per ELM and resulting peak divertor ELM heat flux also are significantly reduced [84]. Deuterium gas injection in the divertor region leads to divertor detachment at similar line-average density as in the conventional divertor, though the radiative volume during detachment, as measured by the bolometer array, appears larger (figure 25); in this detached state at 4.8 s both the steady-state and transient ELM divertor heat pulses measured by infrared thermography, are eliminated, as shown. In this figure, the heat flux profiles at a single toroidal angle are assembled into a 2D image, with red signifying high heat flux (2.5 MW m^{-2}) and blue almost no heat flux.

Joint experiments between DIII-D, C-Mod, and NSTX have produced a coordinated multi-machine database relating measured divertor heat flux profiles to H-mode edge-pedestal parameters over a wide range of conditions [85]. Analysis shows the peak divertor heat flux scaling as $P_{SOL}^{1.2} B_{tor}^{-0.3} B_{pol}^{-1}$ where P is the SOL power and B_{pol} is the midplane poloidal field at the separatrix [86]. These data were recently combined with data from JET and ASDEX [87] to form a more comprehensive database that confirms this trend, suggesting that ITER may have a much narrower midplane T_e profile ($\lambda_q \sim 1$ mm) and higher parallel SOL heat flux than previously expected ($\lambda_q > 5$ mm [88]). However, such a narrow SOL in ITER may imply pressure gradients near the separatrix that would exceed expected edge-pedestal kinetic ballooning-mode

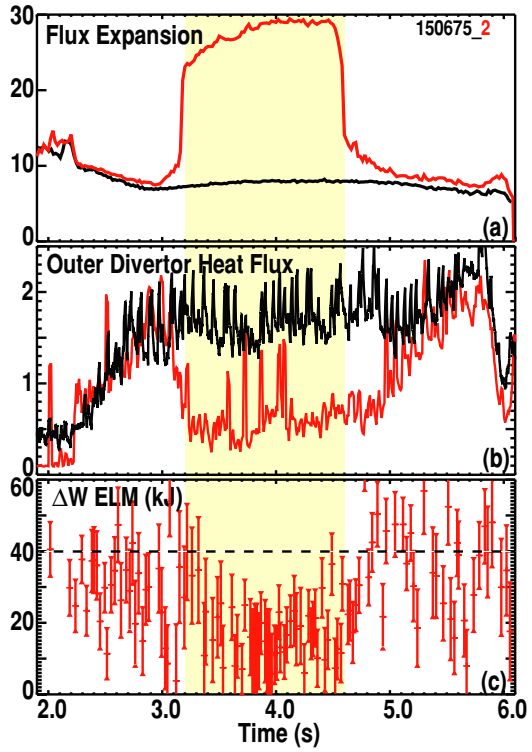

Figure 24. Compared to standard divertor (black), Snowflake-minus (red) increases divertor flux expansion, $B_{\mathrm{pol,mid}}/B_{\mathrm{pol,div}}$, in (*a*); reduces peak inter-ELM heat flux (*b*); and reduces energy loss per ELM in (*c*). Dashed black line in (*c*) shows average ΔW ELM typical of standard divertor configuration in these experiments—replacing actual data to improve clarity.

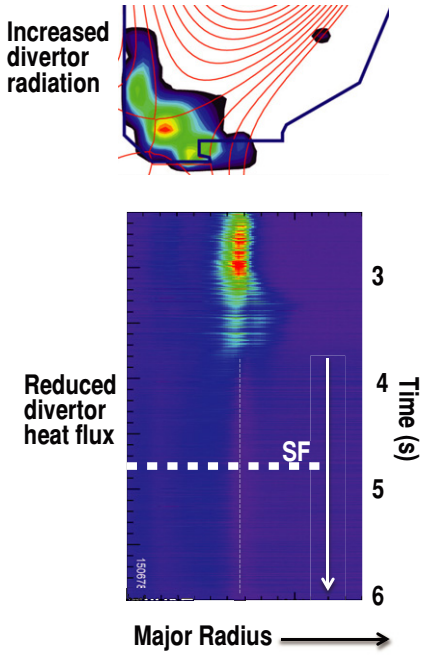

Figure 25. D_2 gas puffing in Snowflake-minus significantly increases radiative power loss in the divertor at 4.8 s (top) and reduces surface heat flux to very low values (bottom), including ELM pulses. Rectangular 2D image of divertor heat flux radial profiles versus time as measured by IR TV (red corresponds to higher heat flux than blue, horizontal dashed line indicates 4.8 s).

stability limits, motivating further experiment and analysis for ITER, as reported in [86].

The all-carbon PFCs in DIII-D make it possible to measure the net surface erosion rate of tungsten in relation to the gross erosion rate in the divertor under realistic conditions using the insertable divertor material exposure system (DiMES) [89]. This ratio is important to understanding and predicting material migration on PFCs in future long-pulse tokamaks. For high-Z target materials such as tungsten, sputtering (the gross erosion) results from bombardment by low-Z ions, such as B, Be, N, or C (as in DIII-D). By exposing well-characterized molybdenum samples to the well-characterized divertor strike-point plasmas in DIII-D ELMing H-mode plasmas and measuring the change in areal surface density of molybdenum, it was possible to determine both the total sputtering and net erosion from the sample, as well as the amount of molybdenum re-deposited nearby. The data shows that the bulk of the sputtered Mo was promptly deposited [90], in agreement with simulations using the DIVIMP Monte Carlo impurity transport code [91]. The results are consistent with assumptions used in calculating the expected net tungsten erosion rates in ITER.

8. Summary and future plans

In this paper we have described recent DIII-D research in a number of areas pertinent to successfully completing design, construction, and operation of ITER, and which support the development of steady-state tokamak reactors.

Prototype $Q = 10$ ITER discharges in DIII-D with low applied torque show that achieving the required performance is possible while using active feedback ECCD for tearing mode control. Advances in pellet pacing and RMP physics move these ELM-control techniques closer to ITER design requirements while strengthening the physics basis for their application; high confinement ELM-free QH-mode can now be obtained over a wide range of applied NBI co- and counter-I_p torque using external $n = 3$ coils. Disruption mitigation experiments point to the possibility of benign RE dissipation with massive gas injection even when well below the Rosenbluth limit.

DIII-D experiments continue to advance the scientific basis for ITER by increasing predictive capability for further system design and scenario optimization as opportunities arise. Key elements of the EPED model describing the H-mode pedestal profile evolution have been confirmed and it is now being used in ELM-control experiments to provide a quantitative basis for relating measured changes in edge profiles to changes in ELM size and frequency. Deployment of a comprehensive set of fast-ion diagnostics, along with OANBI and new 2D fluctuation measurements, has enabled comprehensive tests of simulation codes that will be used to interpret fast-ion stability and transport in ITER. Improved core turbulence measurements and new main-ion rotation profile measurements are enabling more rigorous transport model validation experiments while providing new physics insight to known trends and recognized discrepancies. These results should increase confidence in predicting ITER performance and will likely lead to new ideas for improving it.

Off-axis neutral-beam injection is providing new capability for advancing research aimed towards steady-state

high-beta AT operation needed for fusion energy development. Such operating modes are envisioned for ITER and could form the basis of a future Fusion Nuclear Science Facility (FNSF-AT) [80]. Off-axis neutral-beam injection has enabled operation with $q_{\min} > 2$ to avoid the most unstable tearing modes, and measurably broadened the current profile, yielding significantly higher predicted stability limits ($\beta_N \geqslant 4$) compared to discharges with on-axis NBI only. This potential has yet to be realized because confinement in these discharges is ∼15–20% lower than expected ($H_{98y2} \cong 1$). However, at $q_{\min} = 1.5$ confinement improves and $\beta_N = 3.5$ discharges have been sustained free of low-order tearing modes for more than twice the current relaxation time and come close to meeting the predicted requirements for $Q = 5$ steady-state operation in ITER. In parallel, DIII-D is exploring innovative divertor solutions to address the challenge of steady-state power and particle control.

Future plans seek increased EC power for heating and current drive to improve access to regimes with dominant electron heating, and to improve capability for developing steady-state operating regimes for long-pulse superconducting tokamaks and burning plasma experiments. Commissioning of a 7th long-pulse gyrotron is now under way, with proposed installation of two additional gyrotrons by 2014 to provide increased ECCD power. Other upgrade plans call for additional 3D coil sets and related power supplies in following years. Ongoing modification of existing neutral-beam lines to allow longer pulse lengths will continue in the near term. In the future, we plan to tilt a second beam line to increase capability for AT research.

Acknowledgments

This work was supported by the US Department of Energy under DE-AC52-07NA27344 and DE-FC02-04ER54698.

Appendix: The DIII–D team

G. Abla[1], S. Aekaeslompolo[2], R. Akers[3], S.L. Allen[4], V. Amoskov[5], P.M. Anderson[1], C. Angioni[6], M.E. Austin[7], C. Bae[8], J.P. Bakalarski[1], C.P. Ballance[9], J.E. Barton[10], E.M. Bass[11], D. Battaglia[12], C.B. Baxi[1], L.R. Baylor[13], M. Becoulet[14], E.A. Belli[1], H. Berk[7], J.W. Berkery[15], M.N.A. Beurskens[3], J.M. Bialek[15], N. Bisai[16], J.A. Boedo[11], I.N. Bogatu[17], R.L. Boivin[1], P. Bonoli[18], J.E. Boom[19], A.H. Boozer[15], A. Bortolon[20], M.D. Boyer[10], B.D. Bray[1], D.P. Brennan[21], S. Brezinsek[22], N.H. Brooks[1], J.N. Brooks[23], C. Brunkhorst[12], D. Buchenauer[24], R.V. Budny[12], R. Bulmer[4], K.H. Burrell[1], R.J. Buttery[1], P. Cahyna[25], J.D. Callen[26], R.W. Callis[1], G.L. Campbell[1], J.M. Candy[1], J.M. Canik[13], T.N. Carlstrom[1], T.A. Carter[27], W.P. Cary[1], T.A. Casper[28], M. Cengher[1], C.D. Challis[3], F.R. Chamberlain[1], V.S. Chan[1], C.S. Chang[12], C.S. Chang[29], I.T. Chapman[3], A. Chattopadhyay[16], J.A. Chavez[1], L. Chen[20], Y. Chen[30], H.K. Chiu[1], M. Choi[1], M. Chowduri[16], C. Chrobak[1], C. Chrystal[11], M.S. Chu[1], V. Chuyanov[28], I.G.J. Classen[31], R.H. Coen[4], B. Cohen[4], A.J. Cole[15], S.K. Combs[13], N. Commaux[13], W.A. Cooper[32], N.A. Crocker[27], G. Cunningham[3], S. daGraca[33], R. Daniel[16], J.W. Davis[34], E. delaLuna[35], J.C. DeBoo[1], J.S. deGrassie[1], S.J. DePasquale[12], T.M. Deterly[1], A.Diallo[12], P.H. Diamond[11], S. Diem[13], J.L. Doane[1], C.W. Domier[36], A.J.H. Donne[19], D. Donovan[24], M.A. Dorf[4], M.R. Dorr[4], E.J. Doyle[27], N.W. Eidietis[1], J.D. Elder[34], R. Ellis[4], R.A. Ellis[12], R.F. Ellis[37], T.E. Evans[1], Y. Feng[38], M.E. Fenstermacher[4], N.M. Ferraro[1], J.R. Ferron[1], D.K. Finkenthal[39], R.K. Fisher[1], S.M. Flanagan[1], J.-P. FloydII[8], R.J. Fonck[26], E. Fredd[12], H.G. Frerichs[22], A. Fukuyama[40], S. Futatani[28], J. Garcia[14], M. García-Muñoz[6], A.M. Garofalo[1], R. Geer[4], K.W. Gentle[7], S. Gerhardt[12], G. Giruzzi[14], P. Gohil[1], N.N. Gorelenkov[12], M. Gorelenkova[12], Y.A. Gorelov[1], R.H. Goulding[13], D.L. Green[13], K.L. Greene[1], C.M. Greenfield[1], N.L. Greenough[12], Y. Gribov[28], B.A. Grierson[12], R.J. Groebner[1], W.H. Grosnickle[1], H.J. Grunloh[1], W. Guo[41], T.J. Guzman[1], A.A. Haasz[34], T.S. Hahm[12], S.H. Hahn[42], M.J. Hansink[1], G.R. Hanson[13], J.M. Hanson[15], J.H. Harris[13], R.W. Harvey[43], A. Hassanein[23], N. Hayashi[44], C.C. Hegna[26], W.W. Heidbrink[20], D.N. Hill[4], J.C. Hillescheim[27], D.L. Hillis[13], J.A. Hittinger[4], G.T. Hoang[14], C.T. Holcomb[4], C. Holland[11], E.M. Hollmann[11], K.L. Holtrop[1], M. Honda[44], R.M. Hong[1], A. Horton[13], J.C. Hosea[12], N.T. Howard[18], J. Howard[45], D.M. Hoyt[1], A. Hubbard[18], A. Huber[22], J.W. Hughes[18], D.A. Humphreys[1], P. Huynh[1], G.T.A. Huysmans[28], A.W. Hyatt[1], K. Ida[46], S. Ide[44], F. Imbeaux[14], Y. In[17], R.C. Isler[13], V.A. Izzo[11], G.L. Jackson[1], E.F. Jaeger[13], Y.M. Jeon[42], T.C. Jernigan[13], E.H. Joffrin[14], R.D. Johnson[1], S. Joisa[16], I. Joseph[4], D.H. Kaplan[1], K.M. Keith[1], A.G. Kellman[1], D.H. Kellman[1], C.E. Kessel[12], E.N. Kim[1], J.S. Kim[17], J. E. Kinsey[1], A. Kirk[3], A. Kirschner[22], E. Kolemen[12], M. Kornbluth[47], T. Koskela[48], G.J. Kramer[12], S.I. Krasheninnikov[11], L.P. Ku[12], J.A. Kulchar[1], T. Kurki-Suonio[48], R.J. LaHaye[1], B. LaBombard[18], E. Lamzin[5], M.J. Lanctot[4], L.L. Lao[1], C.J. Lasnier[4], E.A. Lazarus[13], E. Le[7], R.L. Lee[1], X. Lee[1], M. Lennholm[35], A.W. Leonard[1], J.A. Leuer[1], G.Q. Li[41], Z. Lin[20], A. Litnovsky[22], C. Liu[1], Y. Q. Liu[3], D. Liu[26], A. Loarte[28], S.D. Loch[9], L.L. Lodestro[4], N. Logan[12], J. Lohr[1], J.D. Lore[13], T.C. Luce[1], N.C. LuhmannJr.[36], Y. Ma[18], M.A. Mahdavi[49], R. Maingi[13], M.A. Makowski[4], R. Manchanda[16], M. Maraschek[6], A. Marinoni[18], L. Marrelli[50], P. Martin[50], Y. Martin[32], G. Matsunaga[44], P. S. Mauzey[1], D.C. McCune[12], W.L. McDaniel[1], D.C. McDonald[3], B.B. McHarg[1], G.R. McKee[26], A.G. McLean[4], J.E. Menard[12], H. Meyer[3], W.H. Meyer[4], D. Mikkelsen[12], D.C. Miller[1], D. Miller[12], C.P. Moeller[1], S. Mordijck[51], D. Moreau[14], K. Morris[4], E.C. Morse[52], R.A. Moyer[11], S.H. Müller[11], J.M. MuñozBurgos[53], T. Munsat[30], M. Murakami[13], C.J. Murphy[1], C.M. Muscatello[20], Y.-S. Na[54], A. Nagy[12], E. Nardon[14], M.F.F. Nave[55], G.A. Navratil[15], R. Nazikian[12], S. Noraky[1], R.E. Nygren[24], R.C. O'Neill[1], Y.K. Oh[42], S. Ohdachi[46], T. Oikawa[28], M. Okabayashi[12], A. Okamoto[56], R.A. Olstad[1], D.M. Orlov[11], T.H. Osborne[1], Y. Ou[10], L.W. Owen[13], N. Oyama[44], N.A. Pablant[12], D.C. Pace[1], C. Pan[41], H. Pandya[16], A.Y. Pankin[10], G. Park[42], H.K. Park[57], J.K. Park[12], J.M. Park[13], C.T. Parker[1], S. Parker[30], P.B. Parks[1], C.J. Pawley[1], W.A. Peebles[27], B. Pegourie[14], B.G. Penaflor[1], P.I. Petersen[1], T.W. Petrie[1], C.C. Petty[1], N.Q. Pham[1], V. Philipps[22], A.Y. Pigarov[11], D.A. Piglowski[1], R.I. Pinsker[1], P. Piovesan[50], L. Piron[50], R.A. Pitts[28], A. Polevoi[28], P.A. Politzer[1], D.M. Ponce[1], M. Porkolab[18], G.D. Porter[4], R. Prater[1], J.P. Qian[41], R. Rajpal[16],

N. Ramasubramanian[16], D.A. Rasmussen[13], H. Reimerdes[32], D. Reiter[22], Q.L. Ren[41], T.L. Rhodes[27], T.D. Rognlien[4], J.C. Rost[18], D.L. Rudakov[11], P.M. Ryan[13], D.Ryutov[4], S. Saarelma[3], S.A. Sabbagh[15], G. Saibene[58], A. Salmi[48], U. Samm[22], B.S. Sammuli[1], M.E. Sawan[26], M.J. Schaffer[1], D.P. Schissel[1], D.J. Schlossberg[26], O. Schmitz[22], L. Schmitz[27], P. Schneider[6], E. Schuster[10], E. Scime[59], J.T. Scoville[1], M. Shapiro[18], S. Sharapov[3], W. Shi[10], K. Shinohara[44], K.C. Shoolbred[1], P.E. Sieck[1], A.C. C. Sips[6], R.D. Smirnov[11], J.P. Smith[1], S.P. Smith[1], D.R. Smith[26], J.A. Snipes[28], P.B. Snyder[1], E.R. Solano[60], W.M. Solomon[12], A.C. Sontag[13], A.Soppelsa[50], K. H. Spatschek[61], D.A. Spong[13], R. Srinivasan[16], H.E. St. John[1], W.M. Stacey[8], G.M. Staebler[1], R.D. Stambaugh[1], P.C. Stangeby[34], R. Stemprok[1], T. Stevenson[12], H. Stoschus[53], E.J. Strait[1], L. Sugiyama[18], W. Suttrop[6], Y. Suzuki[46], V. Svidzinski[17], T. Tala[2], P. Tamain[14], K. Tanaka[46], R. Tanna[16], D.A. Taussig[1], P.L. Taylor[1], T.S. Taylor[1], G. Taylor[12], D. Temple[3], J.L. Terry[18], D.M. Thomas[1], B.J. Tobias[12], J.F. Tooker[1], D. Truong[26], C.K. Tsui[34], F. Turco[15], A.D. Turnbull[1], G.R. Tynan[11], E.A. Unterberg[13], I.U. Uzun-Kaymak[26], M.A. VanZeeland[1], S. Visser[1], I. Voitsekhovitch[3], F.A. Volpe[15], A. vonHalle[12], M.R. Wade[1], M.L. Walker[1], R.E. Waltz[1], W.R. Wampler[24], G. Wang[27], J.G. Watkins[24], W.P. Wehner[10], A.S. Welander[1], J.C. Wesley[1], R.B. White[12], A.E. White[18], D.G. Whyte[18], S. Wiesen[22], TWilks[8], J.R. Wilson[12], H.R. Wilson[62], A. Wingen[13], E. Wolfrum[6], C.P.C. Wong[1], W. Wu[1], S.J. Wukitch[18], B.J. Xiao[41], X. Xu[4], Z. Yan[26], H.H. Yip[1], S-W. Yoon[42], J.H. Yu[11], Q.P. Yuan[41], G.S. Yun[57], L. Zabeo[28], L. Zeng[27], W. Zhang[27], Y.B. Zhu[20].

[1] General Atomics
[2] Association EURATOM-Tekes, Aalto University, Finland
[3] EURATOM/CCFE Fusion Association, Culham Science Centre
[4] Lawrence Livermore National Laboratory
[5] D.V. Efremove Institute, St. Petersburg, Russia
[6] Max Plank Institut für Plasmaphysik, Garching
[7] University of Texas at Austin
[8] Georgia Institute of Technology
[9] Auburn University
[10] LeHigh University
[11] University of California San Diego
[12] Princeton Plasma Physics Laboratory
[13] Oak Ridge National Laboratory
[14] Associatione Euratom CEA, CEA/DSM/IRFM, Cadarache
[15] Columbia University
[16] Institute for Plasma Research, India
[17] FAR-TECH, Inc.
[18] Massachusetts Institute of Technology
[19] Association EURATOM-FOM Rijnhuizen, The Netherlands
[20] University of California Irvine
[21] University of Tulsa
[22] EURATOM-FZ Jülich
[23] Purdue University
[24] Sandia National Laboratories
[25] IPP, AS CR, EURATOM/IPP.CR, Prague
[26] University of Wisconsin-Madison
[27] University of California Los Angeles
[28] ITER Organization, Cadarache
[29] Courant Institute, New York University
[30] CIPS, University of Colorado, Boulder
[31] Dutch Institute for Fundamental Energy Research
[32] CRPP-EPFL-Lausanne
[33] Association EURATOM-IST, Lisbon
[34] University of Toronto
[35] JET-EFDA-CSU, Abingdon, UK
[36] University of California, Davis
[37] University of Maryland
[38] Max Plank Institut für Plasmaphysik, Greifswald
[39] Palomar College
[40] Kyoto University, Japan
[41] ASIPP-Hefei
[42] National Fusion Research Institute, Korea
[43] CompX
[44] Japan Atomic Energy Agency (JAEA)
[45] Australian National University
[46] National Institute for Fusion Studies
[47] Yeshiva University, New York, NY
[48] Helsinki University of Technology
[49] ALITRON
[50] Consorzio RFX
[51] College of William and Mary, Williamsburg
[52] University of California Berkeley
[53] Oak Ridge Institute of Science Education
[54] Seoul National University, Korea
[55] EURATOM Lisbon
[56] Tohoku University, Sendai, Japan
[57] Pohang University of Science & Technology, Korea
[58] Fusion for Energy Joint Undertaking, Barcelona
[59] West Virginia University
[60] Association EURATOM-CIEMAT, Madrid
[61] Heinrich-Heine University, Düsseldorf
[62] University of York

References

[1] Campbell D.C. 2011 ITER Research Needs, Presentation to the ITPA Coordinating Committee *(Cadarache, France, 12 December 2011)* http://burningplasma.org/ref/ITPACC_campbell_dec11.pdf
[2] Evans T.E. *et al* 2004 *Phys. Rev Lett.* **92** 235003
[3] Evans T.E., Orlov D.M., Wingen A., Wu W., Loarte A., Casoer T.A., Schmitz O., Saibene G. and Schaffer M.J. 2012 *Proc. 24th IAEA Fusion Energy Conf. (San Diego, CA, 2012)* paper ITR/P1-25 www-naweb.iaea.org/napc/physics/FEC/FEC2012/html/fec12.htm
[4] Baylor L.R. *et al* 2012 *Proc. 24th IAEA Fusion Energy Conf. (San Diego, CA, 2012)* paper EX/6-2 www-naweb.iaea.org/napc/physics/FEC/FEC2012/html/fec12.htm
[5] Burrell K.H. *et al* 2001 *Phys. Plasmas* **8** 2153
[6] Wade M.R. *et al Proc. 24th IAEA Fusion Energy Conf. (San Diego, CA, 2012)* paper EX/3-1 www-naweb.iaea.org/napc/physics/FEC/FEC2012/html/fec12.htm
[7] Schaffer M.J. *et al* 2008 *Nucl. Fusion* **48** 024004
[8] Suttrop W. *et al* 2011 *Phys. Rev. Lett.* **106** 225004
[9] Futatani S., Huijsmans G., Loarte A., Baylor L.R., Commaux N., Jernigan T.C., Fenstermacher M.E., Lasnier C.J., Osborne T.H. and Pegourié B. 2012 *Proc. 24th IAEA Fusion Energy Conf. (San Diego, CA, 2012)* paper ITR/P1-22 www-naweb.iaea.org/napc/physics/FEC/FEC2012/html/fec12.htm
[10] Snyder P.B., Osborne T.H., Burrell K.H., Groebner R.J., Leonard A.W., Nazikian R., Orlov D.M., Schmitz O., Wade M.R. and Wilson H.R. 2012 *Phys. Plasmas* **19** 056115

[11] Groebner R.J. *et al* 2001 *Nucl. Fusion* **41** 1789
[12] Snyder P.B. *et al* 2012 *Proc. 24th IAEA Fusion Energy Conf. (San Diego, CA, 2012)* paper TH/P3-17 www-naweb.iaea.org/napc/physics/FEC/FEC2012/html/fec12.htm
[13] Gao L., Balakrishnan S., He W., Yan Z. and Müller R. 2011 *Phys. Rev. Lett.* **107** 214301
[14] Ferraro N.M., Lao L.L., Evans T.E., Moyer R.A., Nazikian R., Orlov D.N., Shafer M.W. and Unterberg E.A. 2013 Edge plasma response to non-axisymmetric fields in tokamaks *Nucl. Fusion* submitted
[15] McKee G.R. *et al* 2012 *Proc. 24th IAEA Fusion Energy Conf. (San Diego, CA, 2012)* paper EX/P7-06 www-naweb.iaea.org/napc/physics/FEC/FEC2012/html/fec12.htm
[16] Hender T.C. *et al* 2007 Progress in the ITER Physics Basis: chapter 3. MHD stability, operational limits and disruptions *Nucl. Fusion* **47** S128
[17] Rosenbluth M.N. and Putvinski S.V. 1997 *Nucl. Fusion* **37** 1355
[18] Hollmann E.M. *et al* 2011 *Nucl. Fusion* **51** 103056
[19] Commaux N. *et al* 2011 *Nucl. Fusion* **51** 103001
[20] Hollmann E.M. *et al* 2010 *Phys. Plasmas* **17** 056117
[21] Hollmann E.M. *et al* 2013 Control and dissipation of runaway electron beams created during rapid shutdown experiments in the DIII-D *Nucl. Fusion* submitted
[22] Eidietis N.W. 2012 *Phys. Plasmas* **19** 056109
[23] Jackson G.L. *et al* 2012 *Proc. 24th IAEA Fusion Energy Conf. (San Diego, CA, 2012)* paper EX/P2-08 www-naweb.iaea.org/napc/physics/FEC/FEC2012/html/fec12.htm
[24] Garofalo A.M. *et al* 2011 *Nucl. Fusion* **51** 083018
[25] Solomon W.M. *et al* 2012 *Proc. 24th IAEA Fusion Energy Conf. (San Diego, CA, 2012)* paper EX/P2-01 www-naweb.iaea.org/napc/physics/FEC/FEC2012/html/fec12.htm
[26] Burrell K.H., Garofalo A.M., Solomon W.M., Fenstermacher M.E., Osborne T.H., Park J.-K. and Snyder P.B. 2012 Reactor-relevant quiescent H-mode operation using torque from non-axisymmetric, non-resonant magnetic fields *Nucl. Fusion* submitted
[27] Cole A.J., Hegna C.J. and Callen J.D. 2007 *Phys. Rev. Lett.* **99** 065001
[28] Garofalo A.M., Burrell K.H., Solomon W.M., Fenstermacher M.E., Hanson J.M., Lanctot M.J., Okabayashi M., Snyder P.B. and the DIII-D Team 2012 *Proc. 39th EPS Conf. on Plasma Physics (Stockholm, SE, 2012)* paper O2.102 and http://ocs.ciemat.es/epsicpp2012pap/html/author.html
[29] Kolemen E., Welander A.S., La Haye R.J., Eidietis N.W., Humphreys D.A., Lohr J., Noraky S., Penaflor B.G., Prater R. and Turco F. 2012 State-of-the-art neoclassical tearing mode control in DIII-D using real-time steerable electron cyclotron current drive launchers *Proc. 24th IAEA Fusion Energy Conf. (San Diego, CA, 2012)* paper PD/1-1 www-naweb.iaea.org/napc/physics/FEC/FEC2012/html/fec12.htm
[30] Nagasaki K., Isayama A., Ide S. and the JT-60 Team 2003 *Nucl. Fusion* **43** L7
[31] La Haye R.J., Isayama A. and Maraschek M. 2009 *Nucl. Fusion* **49** 045005
[32] Volpe F.A., Austin M.E., La Haye R.J., Lohr J., Prater R., Strait E.J. and Welander A.S. 2009 *Phys. Plasmas* **16** 102502
[33] Chapman I.T. *et al* 2012 Assessing the power requirements for sawtooth control in ITER through modelling and joint experiments *Nucl. Fusion* submitted
[34] Buttery R.J. *et al* 2011 *Nucl. Fusion* **51** 073016
[35] Schaffer M.J. *et al* 2011 *Nucl. Fusion* **51** 103028
[36] Buttery R.J. *et al* 2012 *Proc. 24th IAEA Fusion Energy Conf. (San Diego, CA, 2012)* paper EX/P4-31 www-naweb.iaea.org/napc/physics/FEC/FEC2012/html/fec12.htm
[37] Reimerdes H. *et al* 2012 *Proc. 24th IAEA Fusion Energy Conf. (San Diego, CA, 2012)* paper EX/P4-09 www-naweb.iaea.org/napc/physics/FEC/FEC2012/html/fec12.htm
[38] Park J.-K., Boozer A.H. and Glasser A.H. 2007 *Phys. Plasmas* **14** 052110
[39] Buttery R.J. *et al* 2012 *Phys. Plasmas* **19** 056111
[40] Heikkinen J.A. and Sipilä S.K. 1995 *Phys. Plasmas* **2** 724
[41] Kramer G.J. *et al* 2008 *Proc. 22nd Int. Conf. on Fusion Energy 2008 (Geneva, Switzerland, 2008)* CD-ROM _le, IT/P6-3 and http://www-pub.iaea.org/MTCD/Meetings/FEC2008/itp6-3.pdf.
[42] Tani K. *et al* 1981 *J. Phys. Soc. Japan* **50** 1726
[43] Spong D.A. *et al* 1997 *Plasma Phys. Rep.* **23** 483
[44] Kramer G.J. *et al* 2012 *Proc. 24th IAEA Fusion Energy Conf. (San Diego, CA, 2012)* paper ITR/P1-32 www-naweb.iaea.org/napc/physics/FEC/FEC2012/html/fec12.htm
[45] Groebner R.J. *et al* 2013 Improved understanding of physics processes in pedestal structure, leading to improved predictions for ITER *Nucl. Fusion* submitted
[46] Holland C. *et al* 2013 Validation studies of gyrofluid and gyrokinetic predictions of transport and turbulence stiffness using the DIII-D tokamak *Nucl. Fusion* submitted
[47] DeBoo J.C. *et al* 2012 *Phys. Plasmas* **19** 082518
[48] Luce T.C. *et al* 2012 *Proc. 24th IAEA Fusion Energy Conf. (San Diego, CA, 2012)* paper EX/P3-18 www-naweb.iaea.org/napc/physics/FEC/FEC2012/html/fec12.htm
[49] Hillesheim J.C. *et al* 2013 *Phys. Rev. Lett.* **110** 045003
[50] Staebler G.M., Kinsey J.E. and Waltz R.E. 2005 *Phys. Plasmas* **12** 102508
[51] Waltz R.E., Candy J. and Rosenbluth M.N. 2002 *Phys. Plasmas* **9** 1938
[52] White A.E. *et al* 2008 *Phys. Plasmas* **15** 056116
[53] Holland C. *et al* 2009 *Phys. Plasmas* **16** 052301
[54] Rhodes T.L. *et al* 2011 *Nucl. Fusion* **51** 063022
[55] Rhodes T.L. 2011 DOE-FES Joint Research Target *Final Report* http://science.energy.gov/~/media/fes/pdf/fes-presentations/FES_JRT_Report_October_2011.pdf
[56] Waltz R.E. 2012 *Bull. Am. Phys. Soc.* **57** BAPS.2012.DPP.DI3.2
[57] Solomon W.M., Burrell K.H., deGrassie J.S., Boedo J.A., Garofalo A.M., Moyer R.A., Muller S.H., Petty C.C. and Reimerdes H. 2011 *Nucl. Fusion* **51** 073010
[58] Grierson B.A., Burrell K.H. and Solomon W.M. 2012 *Proc. 24th IAEA Fusion Energy Conf. (San Diego, CA, 2012)* paper EX/P3-09 www-naweb.iaea.org/napc/physics/FEC/FEC2012/html/fec12.htm
[59] Grierson B.A., Burrell K.H., Heidbrink W.W., Lanctot M.J., Pablant N.A. and Solomon W.M. 2012 *Phys. Plasmas* **19** 056107
[60] Grierson B.A., Burrell K.H., Solomon W.M., Budny R.V. and Candy J. 2013 Collisionality scaling of main-ion toroidal and poloidal rotation in low torque DIII-D plasmas *Nucl. Fusion* submitted
[61] Doyle E.J. *et al* 2007 Progress in the ITER Physics Basis: chapter 2. Plasma confinement and transport *Nucl. Fusion* **47** S18
[62] Schmitz L. 2012 *Phys. Rev. Lett.* **108** 155002
[63] Conway G. *et al* 2011 *Phys. Rev. Lett.* **106** 065001
[64] Zweben S.J. *et al* 2010 *Phys. Plasmas* **17** 102502
[65] Schmitz L. *et al* 2012 *Proc. 24th IAEA Fusion Energy Conf. (San Diego, CA, 2012)* paper EX/P7-17 www-naweb.iaea.org/napc/physics/FEC/FEC2012/html/fec12.htm
[66] Tynan G. *et al* 2012 *Proc. 24th IAEA Fusion Energy Conf. (San Diego, CA, 2012)* paper EX/10-3 www-naweb.iaea.org/napc/physics/FEC/FEC2012/html/fec12.htm
[67] Yan Z. *et al* 2012 *Proc. 24th IAEA Fusion Energy Conf. (San Diego, CA, 2012)* paper EX/P7-05 www-naweb.iaea.org/napc/physics/FEC/FEC2012/html/fec12.htm
[68] Gohil P. *et al* 2012 *Proc. 24th IAEA Fusion Energy Conf. (San Diego, CA, 2012)* paper ITR/P1-36 www-naweb.iaea.org/napc/physics/FEC/FEC2012/html/fec12.htm
[69] Heidbrink W.W. *et al* 2012 *Proc. 24th IAEA Fusion Energy Conf. (San Diego, CA, 2012)* paper EX/P6-22 www-naweb.iaea.org/napc/physics/FEC/FEC2012/html/fec12.htm

[70] Tobias B.J., Classen I.G.J., Domier C.W., Heidbrink W.W., Luhmann N.C. Jr, Nazikian R., Park H.K., Spong D.A. and Van Zeeland M.A. 2011 *Phys. Rev. Lett.* **106** 075003
[71] Luce T.C. 2011 *Phys. Plasmas* **18** 030501
[72] Murphy C.J. *et al* 2011 *Presented at the IEEE/NPSS 24th Symp. on Fusion Engineering (SOFE), (Chicago, IL, 26–30 June)* pp 1–6 and http://ieeexplore.ieee.org/stamp/stamp.jsp?tp=&arnumber=6052323&isnumber=6052195
[73] Van Zeeland M.A. *et al* 2012 *Proc. 39th EPS Conf. Plasma Physics (Stockholm, Sweden, 2012)* paper P2.068 and http://ocs.ciemat.es/epsicpp2012pap/html/author.html
[74] Park J.M. *et al* 2012 *Proc. 24th IAEA Fusion Energy Conf. (San Diego, CA, 2012)* paper EX/P2-13 www-naweb.iaea.org/napc/physics/FEC/FEC2012/html/fec12.htm
[75] Pankin A., McCune D., Andre R., Bateman G. and Kritz A. 2004 *Comput. Phys. Commun.* **159** 157
[76] Holcomb C.T. *et al* 2012 *Proc. 24th IAEA Fusion Energy Conf. (San Diego, CA, 2012)* paper EX/1-5 www-naweb.iaea.org/napc/physics/FEC/FEC2012/html/fec12.htm
[77] Glasser A.H. and Chance M.S. 1997 *Bull. Am. Phys. Soc.* **42** 1848
[78] Chu M.S., Chance M.S., Glasser A.H. and Okabayashi M. 2003 *Nucl. Fusion* **43** 441
[79] Park J.M. *et al* 2010 *Proc. 23rd Int. Conf. on Fusion Energy (Daejeon, Korea, 2010)* (Vienna: IAEA) CD-ROM file EXC/P2-05 and www.naweb.iaea.org/napc/physics/FEC/FEC2010/html/index.htm
[80] Garofalo A.M. *et al* 2013 A fast-track path to DEMO enabled by ITER and FNSF-AT *Nucl. Fusion* submitted
[81] Moreau D. *et al* 2013 Integrated magnetic and kinetic control of advanced tokamak scenarios based on data-driven models *Nucl. Fusion* submitted
[82] Barton J.E. *et al* 2012 *Proc. 24th IAEA Fusion Energy Conf. (San Diego, CA, 2012)* paper EX/P2-9 www-naweb.iaea.org/napc/physics/FEC/FEC2012/html/fec12.htm
[83] Ryutov D. 2007 *Phys. Plasmas* **14** 064502
[84] Allen S.L. *et al* 2012 Initial snowflake divertor physics studies on DIII-D *Proc. 24th IAEA Fusion Energy Conf. (San Diego, CA, 2012)* paper PD/1-2 www-naweb.iaea.org/napc/physics/FEC/FEC2012/html/fec12.htm
[85] Makowski M.A. *et al* 2012 *Phys. Plasmas* **19** 056122
[86] Makowski M.A. *et al* 2012 *Proc. 24th IAEA Fusion Energy Conf. (San Diego, CA, 2012)* paper EX/P5-16 www-naweb.iaea.org/napc/physics/FEC/FEC2012/html/fec12.htm
[87] Eich T. *et al* 2013 Scaling of the tokamak near scrape-off layer H-mode power width and implications for ITER *Nucl. Fusion* submitted
[88] Loarte A. *et al* 2007 Progress in the ITER Physics Basis: chapter 4. Power and particle control *Nucl. Fusion* **47** S203
[89] Wong C.P.C., Whyte D.G., Bastasz R.J., Brooks J., West W.P. and Wampler W.R. 1998 *J. Nucl. Mater.* **258–263** 433
[90] Rudakov D.L. *et al* 2012 *Proc. 24th IAEA Fusion Energy Conf. (San Diego, CA, 2012)* paper EX/P5-11 www-naweb.iaea.org/napc/physics/FEC/FEC2012/html/fec12.htm
[91] Stangeby P.C. and Elder J.D. 1992 *J. Nucl. Mater.* **196–198** 258